



HAL
open science

The mechanisms shaping CA2 pyramidal neuron action potential bursting induced by muscarinic acetylcholine receptor activation

Vincent Robert, Ludivine Therreau, M. Felicia Davatolhagh, F. Javier Bernardo-Garcia, Katie N Clements, Vivien Chevaleyre, Rebecca Piskorowski

► To cite this version:

Vincent Robert, Ludivine Therreau, M. Felicia Davatolhagh, F. Javier Bernardo-Garcia, Katie N Clements, et al.. The mechanisms shaping CA2 pyramidal neuron action potential bursting induced by muscarinic acetylcholine receptor activation. *Journal of General Physiology*, 2020, 152 (4), pp.e201912462. 10.1085/jgp.201912462 . inserm-02771945

HAL Id: inserm-02771945

<https://inserm.hal.science/inserm-02771945v1>

Submitted on 4 Jun 2020

HAL is a multi-disciplinary open access archive for the deposit and dissemination of scientific research documents, whether they are published or not. The documents may come from teaching and research institutions in France or abroad, or from public or private research centers.

L'archive ouverte pluridisciplinaire **HAL**, est destinée au dépôt et à la diffusion de documents scientifiques de niveau recherche, publiés ou non, émanant des établissements d'enseignement et de recherche français ou étrangers, des laboratoires publics ou privés.

ARTICLE

The mechanisms shaping CA2 pyramidal neuron action potential bursting induced by muscarinic acetylcholine receptor activation

Vincent Robert¹, Ludivine Therreau¹, M. Felicia Davatolhagh², F. Javier Bernardo-Garcia³, Katie N. Clements⁴, Vivien Chevalyre¹, and Rebecca A. Piskorowski¹

Recent studies have revealed that hippocampal area CA2 plays an important role in hippocampal network function. Disruption of this region has been implicated in neuropsychiatric disorders. It is well appreciated that cholinergic input to the hippocampus plays an important role in learning and memory. While the effect of elevated cholinergic tone has been well studied in areas CA1 and CA3, it remains unclear how changes in cholinergic tone impact synaptic transmission and the intrinsic properties of neurons in area CA2. In this study, we applied the cholinergic agonist carbachol and performed on-cell, whole-cell, and extracellular recordings in area CA2. We observed that under conditions of high cholinergic tone, CA2 pyramidal neurons depolarized and rhythmically fired bursts of action potentials. This depolarization depended on the activation of M1 and M3 cholinergic receptors. Furthermore, we examined how the intrinsic properties and action-potential firing were altered in CA2 pyramidal neurons treated with 10 μ M carbachol. While this intrinsic burst firing persisted in the absence of synaptic transmission, bursts were shaped by synaptic inputs in the intact network. We found that both excitatory and inhibitory synaptic transmission were reduced upon carbachol treatment. Finally, we examined the contribution of different channels to the cholinergic-induced changes in neuronal properties. We found that a conductance from K_v7 channels partially contributed to carbachol-induced changes in resting membrane potential and membrane resistance. We also found that D-type potassium currents contributed to controlling several properties of the bursts, including firing rate and burst kinetics. Furthermore, we determined that T-type calcium channels and small conductance calcium-activated potassium channels play a role in regulating bursting activity.

Introduction

While hippocampal area CA2 was first described by Lorente de Nó >70 yr ago (de Nó, 1934), relatively little is known about the cellular properties of the neurons in this region. Recent studies using in vivo recording methods have revealed that neurons in area CA2 play potentially important roles in hippocampal network activity, including initiation of sharp wave ripples (Oliva et al., 2016) and spatial encoding during immobility (Kay et al., 2016). Lesion studies have found that synaptic transmission from area CA2 is required for social recognition memory (Hitti and Siegelbaum, 2014; Stevenson and Caldwell, 2014). Furthermore, there is mounting evidence that this area undergoes detrimental changes during schizophrenia (Benes et al., 1998; Piskorowski et al., 2016), Alzheimer's disease (Ransmayr et al., 1989), Parkinson's disease (Liu et al., 2019), and other neuropsychiatric and neurodegenerative diseases (Chevalyre and Piskorowski, 2016).

To understand the cellular mechanisms underlying these phenomena, the physiological properties of CA2 pyramidal neurons (PNs) require further examination. There is mounting evidence indicating that these neurons have numerous physiological properties that are markedly different from neighboring CA1 and CA3. The calcium buffering and G protein–signaling cascades in these neurons have been shown to actively prevent the expression of stereotypical postsynaptic NMDA-mediated long-term potentiation (Simons et al., 2009; Vellano et al., 2011; Zhao et al., 2007). Additionally, CA2 PNs have been shown to have a very different composition of ion channels and dendritic excitability than neighboring regions (Palacio et al., 2017; Srinivas et al., 2017; Sun et al., 2014; Dudek et al., 2016). CA2 PNs have also been shown to be modulated in the hippocampus by several neuromodulators,

¹Université Paris Descartes, Inserm UMR1266, Institute of Psychiatry and Neuroscience of Paris, Team Synaptic Plasticity and Neural Networks, Paris, France; ²Department of Neuroscience, Perelman School of Medicine, University of Pennsylvania, Philadelphia, PA; ³Department of Biochemistry and Biophysics, University of California San Francisco, San Francisco, CA; ⁴Department of Biology, East Carolina University, Greenville, NC.

Correspondence to Rebecca A. Piskorowski: rebecca.piskorowski@inserm.fr.

© 2020 Robert et al. This article is distributed under the terms of an Attribution–Noncommercial–Share Alike–No Mirror Sites license for the first six months after the publication date (see <http://www.rupress.org/terms/>). After six months it is available under a Creative Commons License (Attribution–Noncommercial–Share Alike 4.0 International license, as described at <https://creativecommons.org/licenses/by-nc-sa/4.0/>).

including oxytocin (Tirko et al., 2018) and vasopressin (Pagani et al., 2015).

The septo-hippocampal cholinergic projection plays a critical role in hippocampal memory formation. Acetylcholine released from septal fibers acts as both a neurotransmitter and a modulator of cellular excitability and synaptic transmission in the hippocampus, thus having wide-ranging effects on hippocampal oscillatory dynamics and synaptic plasticity. In this study, we examined how intrinsic excitability and synaptic transmission are modulated in CA2 PNs under conditions of increased muscarinic tone. We found that under conditions that approximately correspond to awake exploration in vivo (McIntyre et al., 2003; Yamamura et al., 1974), CA2 PNs depolarize and rhythmically fire bursts of action potentials (APs). Activation of M1 and M3 muscarinic receptors is required for the depolarization. We found that excitatory and inhibitory synaptic inputs contributed to the shape and timing of these AP bursts. We observed that burst firing persisted when all synaptic transmission was blocked, indicating that activation of muscarinic acetylcholine receptors altered currents that underlie this phenomenon. To investigate this further, we identified the contribution of K_v7 potassium channels, T-type calcium channels, D-type potassium channels and SK channels to the depolarization and bursting activity of CA2 PNs.

Materials and methods

All procedures involving animals were performed in accordance with institutional regulations.

Slice preparation

Transverse hippocampal slices were prepared from 6–9-wk-old Swiss mice. Animals were anaesthetized with ketamine (100 mg/kg), xylazine (7 mg/kg), and isoflurane and perfused transcardially with an NMDG-based cutting solution containing the following (in mM): NMDG 93, KCl 2.5, NaH_2PO_4 1.25, NaHCO_3 30, HEPES 20, glucose 25, thiourea 2, Na-ascorbate 5, Na-Pyruvate 3, CaCl_2 0.5, and MgCl_2 10. Brains were then rapidly removed, hippocampi were dissected and placed upright into an agar mold and cut into 400- μm -thick transverse slices (Leica VT1200S) in the same cutting solution at 4°C. Slices were transferred to an immersed-type chamber and maintained in artificial cerebral spinal fluid (ACSF) containing the following (in mM): NaCl 125, KCl 2.5, NaH_2PO_4 1.25, NaHCO_3 26, glucose 10, Na-pyruvate 2, CaCl_2 2, and MgCl_2 1. Slices were incubated at 32°C for ~20 min and maintained at room temperature for ≥ 45 min. Before recording, slices were transferred to a recording chamber allowing dual-sided perfusion with ACSF at 5 ml/min at 30°C.

Electrophysiological recordings

All on-cell and whole-cell recordings of CA2 PNs were performed blind. Area CA2 has extremely dense extracellular matrix, making visually guided recordings very challenging. A recording pipette with positive pressure was inserted deeply into the pyramidal cell layer parallel to the stratum so that the tip of the recording pipette was even with the end of the mossy

fibers. The pipette was then stepped deeper into the slice while a voltage step was delivered through the pipette. The current was monitored and used to determine when the pipette was close to a neuron; at that point, positive pressure was released, and a gigaohm seal formed. Cell-attached recordings of CA2 PNs were obtained with ACSF in the recording pipette that had resistances between 2 and 5 $\text{M}\Omega$. Whole-cell recordings were performed with potassium- or cesium-based intracellular solutions containing the following (in mM): K- or Cs-methyl sulfonate 135, KCl 5, EGTA-KOH 0.1, HEPES 10, NaCl 2, MgATP 5, Na_2GTP 0.4, Na_2 -phosphocreatine 10, and biocytin (4 mg/ml). Series resistance was $< 20 \text{ M}\Omega$ and was monitored throughout the recordings. Data were discarded if the series resistance changed $> 10\%$ during the experiment. For synaptic response measurements in voltage-clamp mode, no compensation was applied. In current-clamp mode, the bridge balance was measured every 20 s, compensated with internal circuitry, and monitored throughout experiments as well as before and after gap-free recordings. The liquid junction potential was not corrected for. Data were obtained using a Multiclamp 700B amplifier and digitized using a Digidata 1550 ADDA board. Data were sampled at 10 kHz. pClamp10 software was used for data acquisition.

On-cell and whole-cell current clamp recordings of spontaneous activity were acquired in gap-free mode in sweeps of 10 min. For measurements of intrinsic properties in current clamp mode, direct current (DC) was injected and monitored as necessary to maintain an initial membrane potential (V_M) of -70 mV. AP firing properties were measured with a series of 1-s-long depolarizing current steps.

For voltage-clamp experiments examining evoked and spontaneous synaptic transmission, cesium internal solution was used. Stimulating pipettes filled with ACSF were placed in stratum radiatum of CA1 to antidromically excite CA3-CA2 synapses and in stratum lacunosum moleculare (SLM) to stimulate distal dendritic inputs in area CA2. Synaptic currents were evoked with a constant voltage stimulating unit (Digitimer) set at 0.1 ms at a voltage range of 5–30 V. For minimal stimulation experiments, synaptic responses were evoked by a patch pipette filled with ACSF placed at the same depth as the recording pipette in close proximity to the apical dendrite of the CA2 PN. The stimulus strength (2–10 V, 0.1 ms) was adjusted to elicit small-amplitude excitatory postsynaptic currents (EPSCs; < 20 pA) with $> 10\%$ failure. Extracellular field potentials were recorded with patch pipettes filled with 1 M NaCl placed in CA2 stratum radiatum and SLM for detecting fEPSPs, or in the CA2 pyramidal layer for monitoring spontaneous activity. Pharmacological agents were added to the ACSF at the following concentrations (in μM): 10 carbamoylcholine chloride (CCh) to activate cholinergic receptors; 10 2,3-dihydroxy-6-nitro-7-sulfamoyl-benzo [*f*]quinoxaline (NBQX) and 50 D-2-amino-5-phosphonovalerate (APV) to block α -amino-3-hydroxy-5-methyl-4-isoxazolepropionic acid (AMPA), NMDA, and kainic acid receptors; 1 SR95531 and 2 CGP55845A to block γ -aminobutyric acid (GABA_A and GABA_B) receptors; 10 XE-991 (10,10-bis[4-Pyridinylmethyl]-9[10H]-anthracenone dihydrochloride) to block the M current; 2 TTA-A2 ([*R*]-2-[4-cyclopropylphenyl]-N-[1-[5-[2,2,2-trifluoroethoxy]pyridin-2-yl]ethyl] acetamide) to block T-type voltage-gated

calcium channels; 100 4-aminopyridine (4-AP) to block voltage-activated potassium currents; 0.1 α -dendrotoxin (α -DTX) to block D-type potassium currents; 0.1 apamin to block small-conductance calcium-activated potassium (SK) channels; 10 pirenzepine to block M1 muscarinic receptors; 10 AF-DX 116 to block M2 muscarinic receptors; 1 1,1-dimethyl-4-diphenylacetoxypiperidinium iodide (4-DAMP) to block M3 muscarinic receptors; 10 mecamylamine to block nicotinic acetylcholine receptors (nAChRs); and 0.1 tetrodotoxin (TTX) to block voltage-activated sodium channels. Voltage clamp recordings of miniature excitatory postsynaptic currents (mEPSCs) were performed with 100 nM TTX and 4 mM CaCl_2 in ACSF.

Immunocytochemistry and cell identification

Post hoc confirmation of all cells was performed by reconstruction of neuronal morphology. Following overnight incubation in 4% paraformaldehyde in PBS, slices were permeabilized with 0.2% Triton X-100 in PBS and blocked for 48 h with 3% goat serum in PBS with 0.2% Triton X-100. Alexa Fluor 546-conjugated streptavidin (Life Technologies, dilution 1:300) incubation was performed in block solution for 4 h at room temperature. Slices were mounted in prolong diamond mounting medium, resulting in a partial clarification of tissue following incubation at room temperature for 24 h. Images were collected with a Zeiss 710 laser-scanning confocal microscope.

Data analysis

Electrophysiological recordings were analyzed using custom-written macros with IGORpro (Wavemetrics) and Axograph software. APs were detected automatically by threshold crossing with IGOR TaroTools, followed by visual inspection to define AP bursts. In all whole-cell recordings, bursts were defined by clear depolarization and repolarization of the V_M flanking AP firing. For analysis of cell-attached data, bursts were defined based on the shortest bursts with lowest interburst interval seen in whole-cell recordings. This was defined as groups of ≥ 2 APs occurring < 1 s apart from one another and separated from other groups of APs by ≥ 1 s. While this definition is broad, we used it to avoid constraining the analysis of cell-attached data. Kinetics of V_M variations were measured by linear fits of the V_M trace as it changed during the initial depolarization following CCh application, and from interburst- V_M plus 5 mV to burst- V_M minus 5 mV. Membrane resistance (R_M) measurements were calculated from linear fits of the voltage responses to current step injections. AP firing properties were measured on a positive current step 1.5 times over rheobase causing similar V_M depolarization for each cell and condition, typically 200 pA over rheobase. The threshold was measured at the first AP at rheobase. The AP full-width at half-maximal amplitude (AP width) and afterhyperpolarizing potential (AHP) amplitude were measured for the first AP at threshold. The latency of the first AP and number of APs was measured with increasing current steps over rheobase. The instantaneous firing frequency and amplitude of the first six APs were measured at current injection steps 1.5 times over rheobase. The amplitude of the afterdepolarization (ADP) was measured 125 ms after step termination of a current 1.5 times over rheobase. Sag potentials

were measured with a protocol injecting current as necessary to maintain a V_M of -70 mV with a 1-s-long negative current step resulting in a membrane hyperpolarization of -100 mV. The sag was calculated as the difference between the peak and steady-state voltage during the 1-s hyperpolarization.

Statistics

Results are reported as means \pm SEM. Statistical significance of linear variables was assessed using paired or unpaired Student's *t* test, one-sample *t* test, Mann-Whitney *U* test, Wilcoxon signed-rank test, Kruskal-Wallis test, one-way ANOVA, repeated-measures ANOVA, or Friedman ANOVA where appropriate. Normality was tested with the Jarque-Bera test, and homoscedasticity was tested using Barlett's test to choose between parametric and nonparametric statistical analysis. The marks *, **, and *** denote *P* values < 0.05 , < 0.01 , and < 0.001 , respectively.

Results

Carbachol induces depolarization and AP bursting in CA2 PNs

Modulation of hippocampal neuronal activity by cholinergic agonists has been extensively described for PNs in areas CA3 and CA1. However, little is known about how activity in area CA2 is affected by increased muscarinic tone. To answer this question, we performed on-cell electrophysiological recordings in CA2 PNs in acute hippocampal slices from adult mice and monitored how the activity of the cells changed upon the application of 10 μM carbachol (CCh). This compound is the carbamate analogue of acetylcholine, allowing it to resist hydrolysis by acetylcholinesterase, and is a nonselective agonist for muscarinic acetylcholine receptors and a weaker nonselective agonist for nAChRs in the brain. We found that before CCh application, only 1 of 15 cells spontaneously fired APs. Following application of 10 μM CCh, 8 of 15 cells displayed regularly repeating bursts of APs (Fig. 1, A1 and A2). Within each burst, the cells fired 14.6 ± 2.2 APs at a frequency of 14.3 ± 4.2 Hz. Each burst lasted 6.4 ± 2.1 s, with an interburst interval of 90 ± 38 s.

The spontaneous rhythmic firing of bursts of APs that we observed in area CA2 are similar to previous reports of CA3 PNs following application of CCh (MacVicar and Tse, 1989; Williams and Kauer, 1997; Cobb et al., 1999; Cobb and Davies, 2005). We postulated that high muscarinic tone may be causing a change in the resting V_M in CA2 PNs, as has previously been reported in area CA3 (Dodd and Kelly, 1981; Cobb et al., 1999; Cobb and Davies, 2005) and in CA2 pyramidal cells in slice cultures (Fischer, 2004). To answer this question, we performed whole-cell current clamp recordings before and after bath-application of 10 μM CCh. Upon CCh application, we observed a depolarization of CA2 PN V_M from rest at -75 ± 1.1 mV to -65 ± 1.0 mV (Fig. 1, B1-B3; $n = 29$; paired *t* test, $P < 0.001$). CCh application caused V_M depolarization at a rate of 6.0 ± 0.7 mV/min ($n = 29$) before reaching a steady-state level. This depolarization was followed by rhythmic bursts of AP firing in 25 of 29 cells, with properties similar to those we observed in cell-attached recordings. We restricted the analysis of our whole-cell data to 15 min following CCh application because the on-cell data from

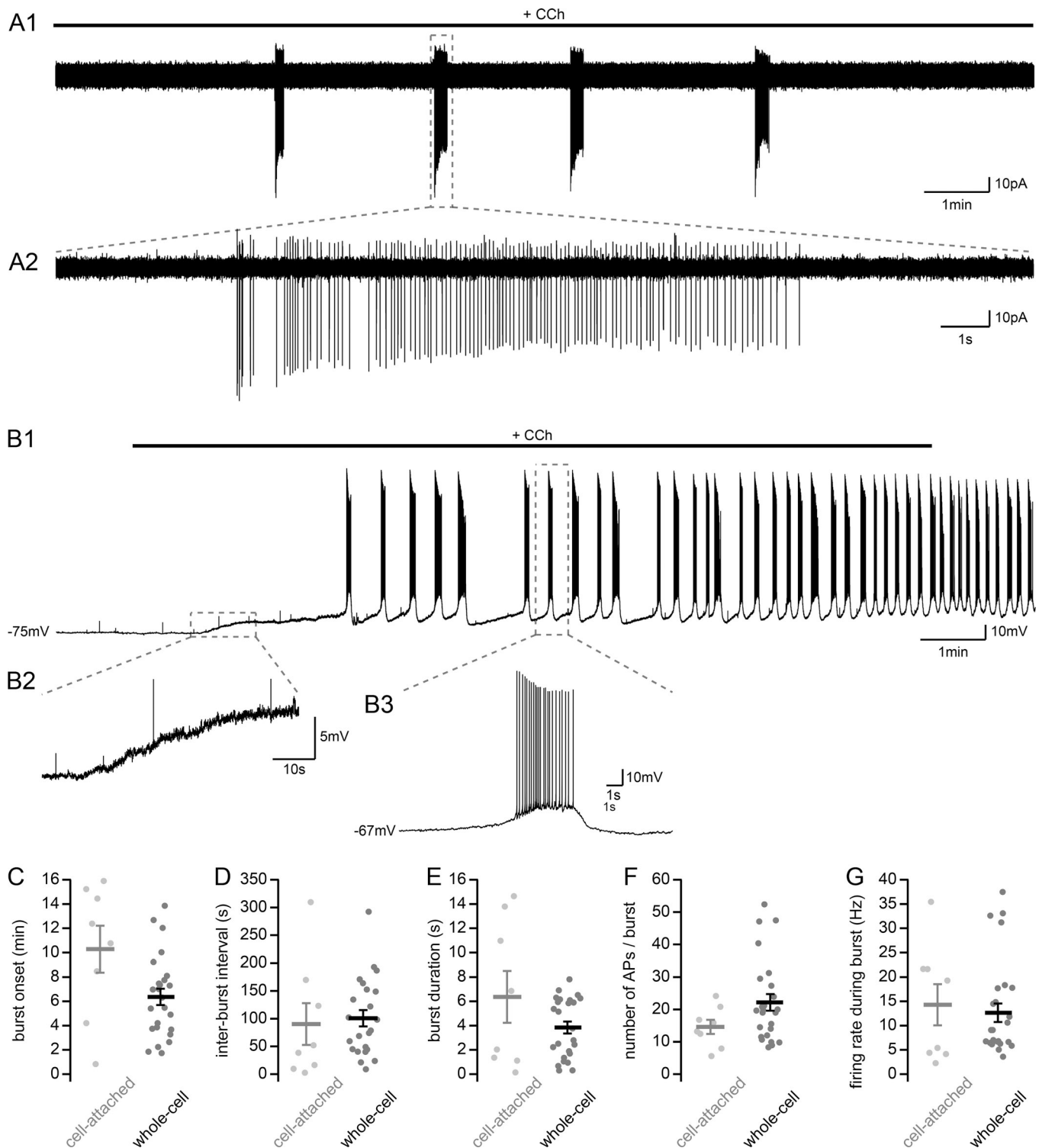


Figure 1. **Carbachol application induces V_M depolarization and burst firing in CA2 PN.** (A1) Sample trace of AP bursts recorded in cell-attached configuration from a putative CA2 PN following application of $10 \mu\text{M}$ CCh in acute hippocampal slice. (A2) Expanded view of a single burst of APs. (B) Sample trace of bursts recorded in whole-cell current-clamp configuration from a CA2 PN upon application of $10 \mu\text{M}$ CCh in acute hippocampal slice (B1) and expanded views of the V_M initial depolarization (B2) and a burst of APs (B3). (C–G) Summary graphs of burst properties recorded in cell-attached (gray, $n = 8$) and whole-cell current-clamp (black, $n = 25$) configuration from CA2 PN with application of $10 \mu\text{M}$ CCh (individual cells shown as dots; population averages shown as thick lines; error bars represent SEM). (C) Bursting onset (cell-attached, 10.3 ± 1.9 min; whole-cell, 6.4 ± 0.7 min; t test, $P = 0.088$). (D) Interburst interval (cell-attached, 90 ± 38 s; whole-cell, 100 ± 14.7 s; t test, $P = 0.80$). (E) Burst duration (cell-attached, 6.4 ± 2.1 s; whole-cell, 3.8 ± 0.5 s; Mann–Whitney U test, $P = 0.48$). (F) Number of APs per burst (cell-attached, 14.6 ± 2.2 ; whole-cell, 22 ± 2.5 ; Mann–Whitney U test, $P = 0.17$). (G) Firing rate during burst (cell-attached, 14.3 ± 4.2 Hz; whole-cell, 12.6 ± 1.9 Hz; Mann–Whitney U test, $P = 0.71$).

bursting cells showed that cells would burst during this time window. Furthermore, we wanted to avoid variation of cellular properties due to dialysis of the cytoplasm from whole-cell recording conditions. The fraction of bursting cells recorded in cell-attached ($n = 8/15$) and whole-cell ($n = 25/29$) configurations were not statistically different (chi-square test, $P = 0.127$). Bursting occurred 10.3 ± 1.9 min ($n = 8$) after CCh application in cell-attached mode and after 6.4 ± 0.7 min ($n = 25$) in whole-cell recordings (Fig. 1 C). Bursts occurred with an interburst interval of 100 ± 14.7 s (Fig. 1 D) and lasted 3.8 ± 0.5 s (Fig. 1 E). During these bursts, CA2 PNs fired 22 ± 2.5 APs paced at 12.6 ± 1.9 Hz (Fig. 1, F–G). Importantly, none of the measurements reported above differed between cell-attached and whole-cell conditions, thus validating our approach. Following each burst of AP-firing, the V_M returned to an interburst potential that was significantly more depolarized than before CCh application of -62.3 ± 0.8 mV (paired t test, $P < 0.001$).

We further studied the CCh-induced initial depolarization seen in whole-cell recordings before bursting. $10 \mu\text{M}$ CCh depolarized CA2 PN V_M within minutes of application (Fig. 2 A, $n = 25$ cells that subsequently fired bursts of APs; Fig. 2 B, $n = 29$ cells recorded in $10 \mu\text{M}$ CCh). This depolarization of the V_M following application of $10 \mu\text{M}$ CCh is likely acting via mAChRs, G-protein coupled metabotropic receptors that are expressed in the soma, dendrites, and axonal terminals of hippocampal PNs (Pitler and Alger, 1990; Levey et al., 1995). We found that with prior application of $10 \mu\text{M}$ pirenzepine, which will preferentially act on M1 receptors with partial antagonism of M3 receptors, CCh application resulted in a minor membrane depolarization of 1.6 ± 0.7 mV that was significantly lower than the 10.0 ± 0.9 mV depolarization observed in CCh alone (Fig. 2 B). Further, application of $10 \mu\text{M}$ AF-DX 116, an M2 receptor antagonist, had no significant effect on the CCh-induced depolarization (Fig. 2 B; 7.7 ± 1.1 mV). Application of $1 \mu\text{M}$ 4-DAMP, which should primarily act on M3 mAChRs but also a fraction of M1 mAChRs, also effectively prevented CCh-induced depolarization, resulting in a small depolarization (Fig. 2 B; 2.1 ± 0.5 mV). Consequently, CCh-induced AP bursting of CA2 PNs was blocked by pirenzepine and 4-DAMP but not by AF-DX 116 (Fig. 2 C). These results were consistent with the $G_{q/11}$ -coupled action of M1 and M3 receptors, which is known to inhibit potassium permeability, leading to membrane depolarization (Brown and Adams, 1980).

Next, we explored the dose-dependent effects of CCh on CA2 PNs and performed experiments with CCh concentrations ranging from 0.5 to $20 \mu\text{M}$ (Fig. 2, D1–D3). These experiments showed that, although application of $10 \mu\text{M}$ CCh robustly depolarized CA2 PNs, CCh concentrations as little as $0.5 \mu\text{M}$ significantly depolarized CA2 PNs (Fig. 2, E and F). However, AP bursts were observed consistently with CCh concentrations of $\geq 10 \mu\text{M}$ (Fig. 2 G). While burst firing was observed with lower concentrations, these occurred in only a fraction of experiments. Measurements of acetylcholine that have been performed in the hippocampus in vivo indicate that the concentration of acetylcholine during awake exploration is in the range of 0.5 – $1 \mu\text{M}$ (10 – 20 pmol acetylcholine/ $20 \mu\text{l}$ CSF; McIntyre et al., 2003). Because CCh affinity for mAChRs is 10-fold lower than that of acetylcholine (Yamamura et al., 1974),

and because $10 \mu\text{M}$ CCh falls within this physiological range and consistently provokes bursts of AP firing, we used this concentration for the rest of the study.

To better understand how CA2 PN intrinsic properties and AP firing are altered by muscarinic tone, we performed whole-cell current clamp experiments. Current step injections before and after $10 \mu\text{M}$ CCh application revealed that many aspects of CA2 PN intrinsic properties and AP firing behavior were modified by CCh (Fig. 3, A1–A4). For these experiments, we took care to inject DC as necessary to maintain an initial V_M of -70 mV. First, we found that CCh application significantly increased CA2 PN R_M from 42 ± 2.8 to 90 ± 8.0 M Ω (Fig. 3 B). We examined several aspects of AP firing. We observed an increased AP threshold, from -47.0 ± 0.9 to -44.0 ± 0.8 mV (Fig. 3 C). Furthermore, we saw a decreased AP width, from 1.13 ± 0.04 to 1.02 ± 0.04 ms (Fig. 3 D), and an increased AHP from 6.2 ± 0.6 to 8.3 ± 0.4 mV (Fig. 3 E). In addition, the latency of first AP firing during a step was increased following CCh application, from 83 ± 11 to 156 ± 15 ms. The latency was compared at a current injection step 200 pA over rheobase (Fig. 3 F). At the same current injection, the number of APs per step also increased from 5.0 ± 0.5 to 11.9 ± 1.1 (Fig. 3 G). This increase is consistent with a decrease in AP duration and increase in AHP. CCh application also resulted in increased instantaneous AP frequency, which was measured from the first and second AP, from 15.9 ± 1.8 to 19.6 ± 2.1 Hz (Fig. 3 H). With this, we noticed that CCh prevented adaptation of AP firing frequency with increasing current injection steps. We measured a decreased AP amplitude, from 77.5 ± 1.4 to 71.1 ± 2.4 mV, following CCh application (Fig. 3 I). Following the termination of current steps eliciting AP firing, we observed an increased ADP of 7.0 ± 0.9 mV in CCh compared with 1.6 ± 0.3 mV in ACSF (Fig. 3, J and K). Finally, we observed that the sag potential measured following a hyperpolarizing step to -100 mV in CA2 PNs was increased by CCh application from 1.6 ± 0.1 mV to 4.5 ± 0.5 mV (Fig. 3, L and M). These results suggest that several conductances are modulated by CCh in CA2 PNs.

CA2 PN AP bursts are shaped by synaptic inputs

Muscarinic AChR activation has been shown to alter both synaptic transmission and ionic conductances that regulate intrinsic excitability in PNs and interneurons (Cobb and Davies, 2005; McQuiston, 2014). In area CA3, many of the properties of rhythmic burst-firing have been shown to be shaped by changes in the local inhibitory and recurrent excitatory network (Williams and Kauer, 1997; McMahan et al., 1998). For area CA2, the effect of CCh on both the local network activity and intrinsic properties has never been examined. To better understand the CCh-induced spontaneous activity in area CA2, we set out to evaluate the contribution of synaptic input to several properties of spontaneous AP bursting (Fig. 4 A). First, we assessed the contribution of excitatory transmission in CA2 PN bursting by blocking fast glutamatergic transmission with $10 \mu\text{M}$ NBQX and $50 \mu\text{M}$ APV. We saw that under these conditions, CA2 PNs continued to burst (Fig. 4, A2). We observed a significantly shorter interburst interval (Fig. 4 B and Table 1) and postulate that this is due to the significantly more depolarized V_M between bursts (Fig. 4 G and Table 1). Furthermore, with the block of

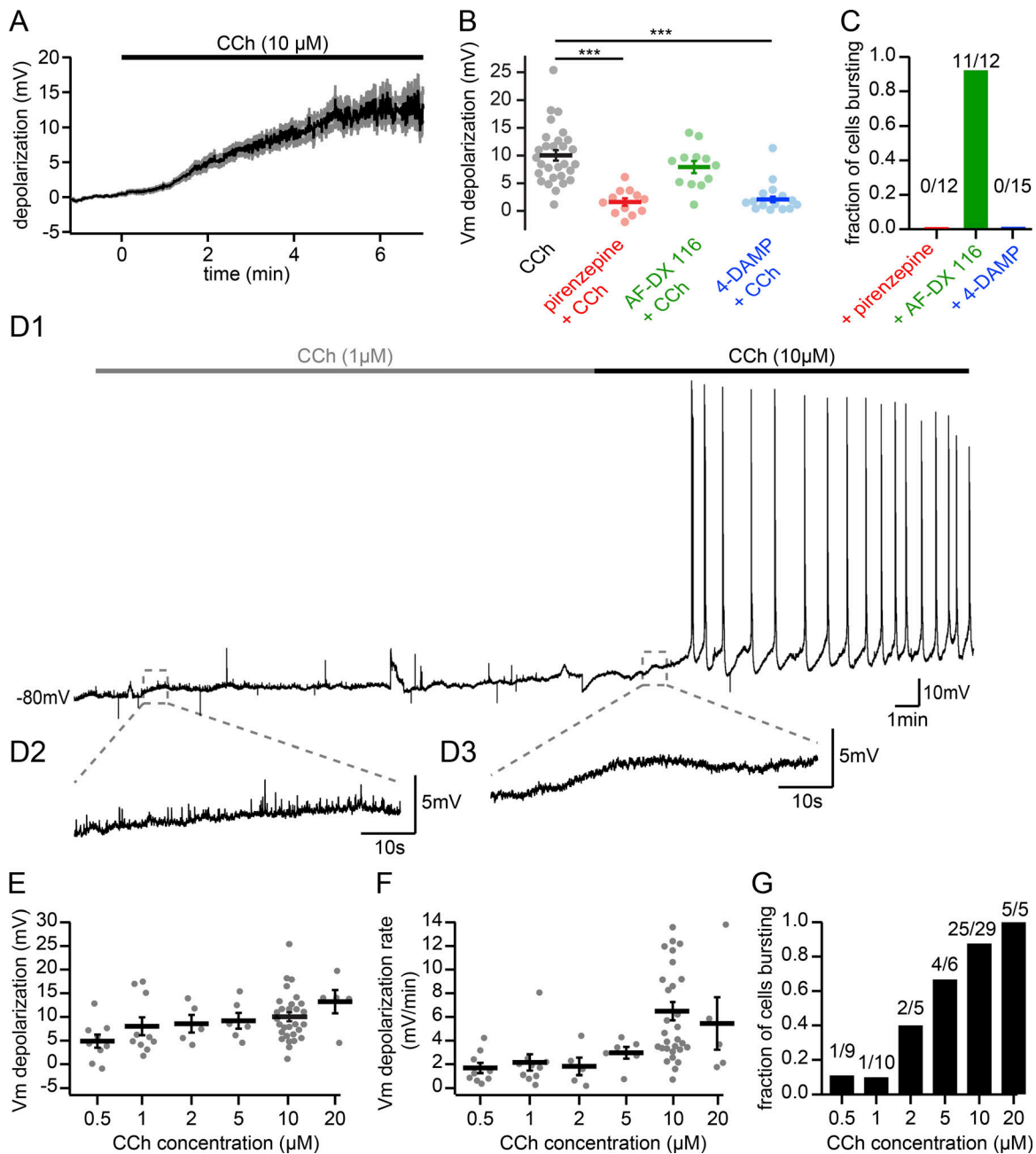


Figure 2. Depolarization of CA2 PN resting V_M by CCh. (A) Time course of the initial V_M depolarization leading to bursting onset following 10 μM CCh application ($n = 25$; population average shown as black line; gray region represents SEM). (B) Summary graph of V_M depolarization before and after application of 10 μM CCh in control conditions or with muscarinic acetylcholine receptors M1, M2, or M3 blocked by 10 μM pirenzepine, 10 μM AF-DX 116, or 1 μM 4-DAMP, respectively. The depolarization induced by CCh (black, $n = 29$) was significantly reduced by pirenzepine (red, Mann-Whitney U test, $p < 0.001$, $n = 12$) and 4-DAMP (blue, Mann-Whitney U test, $P < 0.001$, $n = 15$) but not by AF-DX 116 (green, Mann-Whitney U test, $P = 0.185$, $n = 12$; individual cells shown as dots; population averages shown as thick lines; error bars represent SEM). ***, $P < 0.001$. (C) Fraction of cells that burst following application of 10 μM CCh and in the presence of pirenzepine, AF-DX 116, or 4-DAMP (chi-squared test, $P < 0.001$). (D) Sample trace recorded in whole-cell current-clamp configuration from a CA2 PN (D1) and expanded view showing a small V_M depolarization without bursts during application of 1 μM CCh followed by further depolarization (D2) and AP bursts upon subsequent increased CCh concentration to 10 μM in acute hippocampal slice (D3). (E-G) Summary graphs of the initial V_M depolarization and subsequent bursting as a function of increasing CCh concentrations (0.5 μM , $n = 9$; 1 μM , $n = 10$; 2 μM , $n = 5$; 5 μM , $n = 6$; 10 μM , $n = 29$; 20 μM , $n = 5$; individual cells shown as dots; population averages shown as thick lines; error bars represent SEM). (E) Initial V_M depolarization induced by CCh (one-sample t tests: 0.5 μM , $P = 0.0079$; 1 μM , $P = 0.0022$; 2 μM , $P = 0.010$; 5 μM , $P = 0.0026$; 10 μM , $P < 0.001$; 20 μM , $P = 0.0056$). (F) Initial V_M depolarization rate during CCh application. (G) Fraction of cells bursting during CCh application (chi-square test, $P = 0.002$).

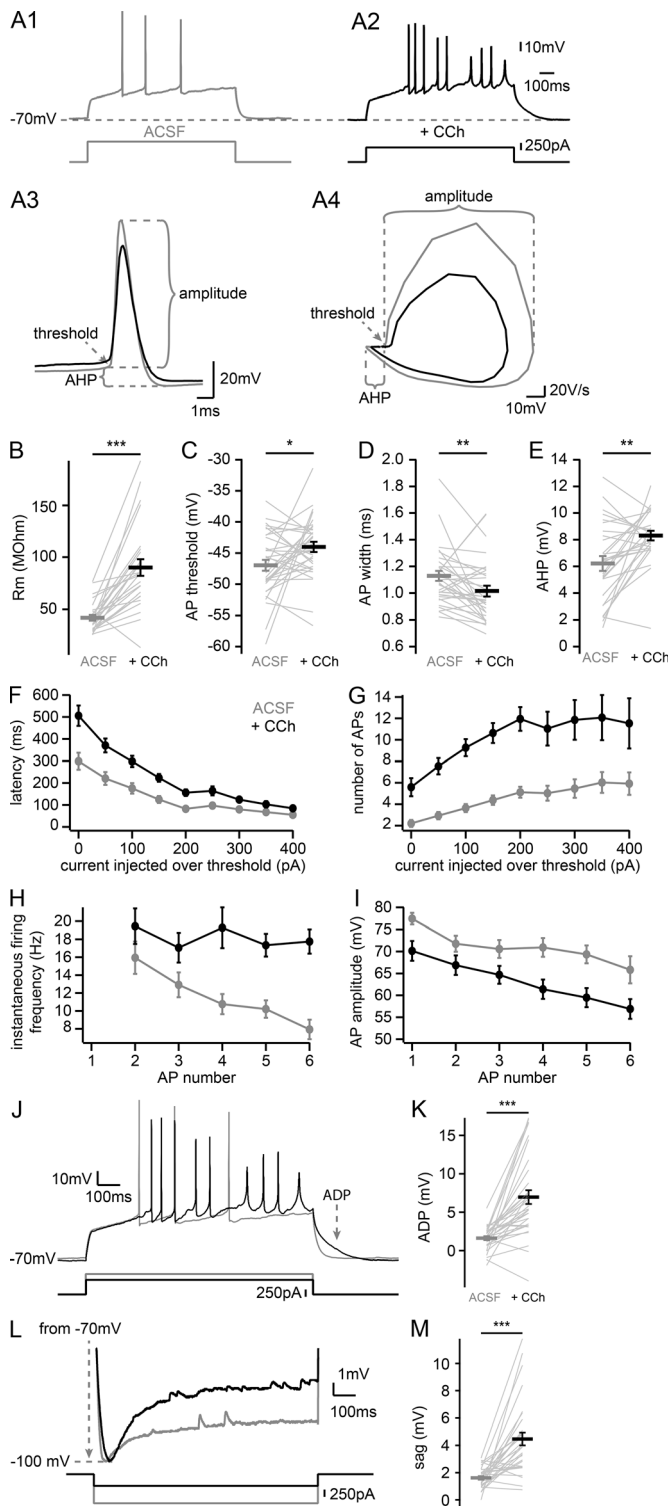


Figure 3. Modification of CA2 PN intrinsic properties by CCh. (A) Sample traces of AP firing in response to depolarizing current step injections recorded in whole-cell current-clamp configuration from a CA2 PN in control (A1, gray) and 10 μM CCh (A2, black), expanded view of the first AP in each condition (A3) and corresponding phase plane plot (A4). (B–I) Summary graphs of CA2 PNs AP firing properties in control (gray) and 10 μM CCh (black; individual cells shown as thin lines, population averages shown as thick lines, error bars represent SEM). (B) R_M (before CCh, 42 ± 2.8 MOhm; after CCh, 90 ± 8.0 MOhm; Wilcoxon signed-rank test, $P < 0.001$, $n = 26$). (C) AP threshold (before CCh, -47.0 ± 0.9 mV; after CCh, -44.0 ± 0.8 mV;

excitatory transmission, we observed a significant decrease in the number of APs per burst (Fig. 4 D and Table 1), indicating that synaptic input from CA2 and CA3 PNs plays a significant role in the spontaneous activity. A possible consequence of blocking excitatory transmission is that less sustained AP firing during bursts would cause a decrease in activation of hyperpolarizing conductances, potentially leading to reduced repolarization of CA2 PN V_M following bursts.

Area CA2 has been shown to have a very high density of interneurons with unique morphologies and axonal projection patterns (Mercer et al., 2007, 2012; Botcher et al., 2014). To assess the contribution of the local inhibitory network to CCh-induced CA2 PN spontaneous AP bursting, we blocked all GABA_A and GABA_B receptors by applying 1 μM SR95531 and 2 μM CGP55845A. We observed several notable changes following CCh application under these conditions. The burst duration was significantly shorter (Fig. 4 C and Table 1) resulting in a trend for less AP fired per burst (Fig. 4 D and Table 1), although the firing rate during a burst was significantly higher (Fig. 4 E and Table 1) than in control conditions with GABAergic transmission intact. Furthermore, the rate of depolarization preceding a burst, burst rise rate, was significantly faster (Fig. 4 H and Table 1) and the rate at which the V_M hyperpolarized following a burst, the burst decay rate, tended to be faster, although the difference was not significant (Fig. 4 I and Table 1). Our interpretation of these results is that local inhibition is acting to pace AP firing during bursts in CA2 PNs in the presence of CCh. Furthermore, the local field potential (LFP) recorded nearby in the pyramidal layer of area CA2 bore signatures of epileptiform-like events (Fig. 4 A3). These events consisted of brief (0.8 ± 0.3 s, $n = 5$) bursts of 3.3 ± 1.3

Wilcoxon signed-rank test, $P = 0.017$, $n = 34$). (D) AP width at half-maximal amplitude (before CCh, 1.13 ± 0.04 ms; after CCh, 1.02 ± 0.04 ms; Wilcoxon signed-rank test, $P = 0.005$, $n = 34$). (E) AHP (before CCh, 6.2 ± 0.6 mV; after CCh, 8.3 ± 0.4 mV; Wilcoxon signed-rank test, $P = 0.002$, $n = 29$). (F) Latency to fire first AP per current step as a function of current injection over rheobase (200 pA over rheobase, before CCh, 83 ± 11 ms; after CCh, 156 ± 15 ms; Wilcoxon signed-rank test, $P < 0.001$, $n = 34$). (G) Number of APs fired per current step as a function of current injection over rheobase (200 pA over rheobase, before CCh, 5.0 ± 0.5; after CCh, 11.9 ± 1.1; Wilcoxon signed-rank test, $P < 0.001$, $n = 34$). (H) Instantaneous firing frequency of APs as a function of AP number during a current step of intensity chosen 1.5 times above rheobase (first couple of APs, before CCh, 15.9 ± 1.8 Hz; after CCh, 19.6 ± 2.1 Hz; Wilcoxon signed-rank test, $P = 0.027$, $n = 31$). (I) AP amplitude as a function of AP number during a current step of intensity chosen 1.5 times above rheobase (first AP, before CCh, 77.5 ± 1.4 mV; after CCh, 71.1 ± 2.4 mV; paired t test, $P = 0.020$, $n = 29$). (J) Sample traces of the ADP following a depolarizing current step injection in a CA2 PN recorded in whole-cell current-clamp configuration in control (gray) and 10 μM CCh (black). (K) Summary graph of CA2 PNs ADP in control (gray) and 10 μM CCh (black; before CCh, 1.6 ± 0.3 mV; after CCh, 7.0 ± 0.9 mV; paired t test, $P < 0.001$, $n = 34$; individual cells shown as thin lines; population averages shown as thick lines; error bars represent SEM). (L) Sample traces of voltage sag in response to hyperpolarizing current step injections recorded in whole-cell current-clamp configuration from a CA2 PN in control (gray) and 10 μM CCh (black). (M) Summary graph of CA2 PN voltage sag following hyperpolarization to -100 mV in control ACSF (gray) and 10 μM CCh (black; before CCh, 1.6 ± 0.1 mV; after CCh, 4.5 ± 0.5 mV; Wilcoxon signed-rank test, $P < 0.001$, $n = 31$; individual cells shown as thin lines; population averages shown as thick lines; error bars represent SEM). *, $P < 0.05$; **, $P < 0.01$; ***, $P < 0.001$.

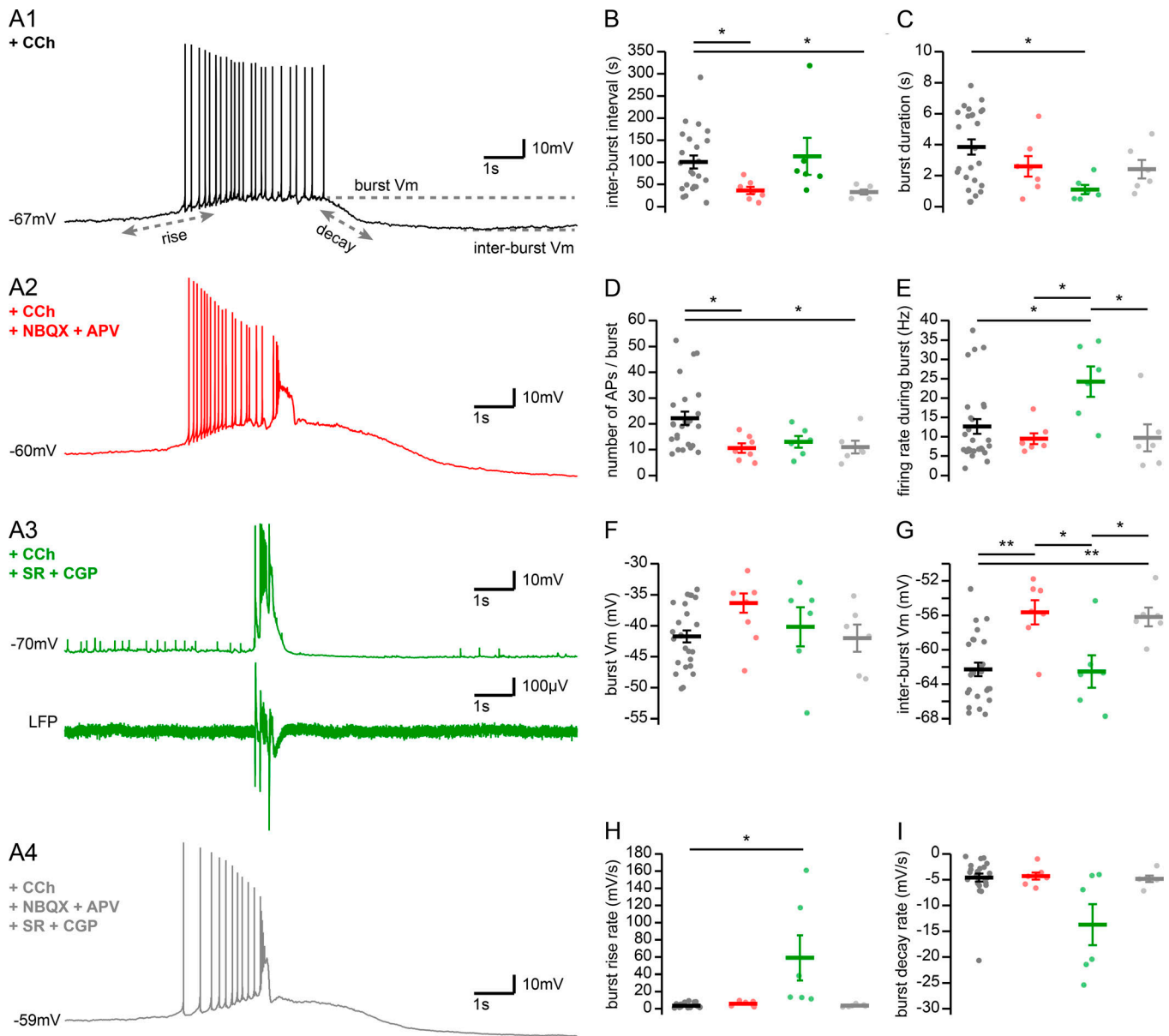


Figure 4. Contribution of synaptic transmission to CCh-induced AP burst firing in CA2 PN. (A) Sample trace of bursts recorded in whole-cell current-clamp configuration from a CA2 PN upon application of 10 μ M CCh in acute hippocampal slice in control condition (A1, 10 μ M CCh, black) or application of 10 μ M NBQX and 50 μ M APV (A2, red); 1 μ M SR95531 and 2 μ M CGP5584A (A3, green); and 10 μ M NBQX, 50 μ M APV, 1 μ M SR95531, and 2 μ M CGP5584A (A4, gray). A3 shows an additional trace of an epileptiform-like discharge recorded in CA2 *stratum pyramidale* (LFP, lower trace). (B–I) Summary graphs of burst characteristics with application of 10 μ M CCh in control (black, $n = 25$; same CCh data shown in B–E as whole-cell data in Fig. 1, D–G, respectively); 10 μ M NBQX and 50 μ M APV (red, $n = 7$); 1 μ M SR95531 and 2 μ M CGP5584A (green, $n = 6$); and 10 μ M NBQX, 50 μ M APV, 1 μ M SR95531, and 2 μ M CGP5584A (gray, $n = 6$; individual cells shown as dots; population averages shown as thick lines; error bars represent SEM). (B) Interburst interval (Kruskal–Wallis test, $P = 0.006$). (C) Burst duration (Kruskal–Wallis test, $P = 0.037$). (D) Number of APs per burst (Kruskal–Wallis test, $P = 0.008$). (E) AP firing frequency during bursts (Kruskal–Wallis test, $P = 0.012$). (F) V_m level during bursts (one-way ANOVA, $P = 0.41$). (G) V_m level in between bursts (one-way ANOVA, $P < 0.001$). (H) V_m depolarization rate during the burst rising phase (Kruskal–Wallis test, $P < 0.001$). (I) V_m repolarization rate during the burst decaying phase (Kruskal–Wallis test, $P = 0.087$). *, $P < 0.05$; **, $P < 0.01$.

synaptic potentials with superimposed population-spike-like signals. We detected these events in five of six CA2 PN recorded in the presence of GABA blockers. In these PN, epileptiform-like discharges accompanied 70 \pm 8% of the AP bursts, which they tended to precede by 32 \pm 12 ms. Our interpretation of this activity is that with inhibitory transmission blocked, PN in the network undergo AP bursting that is not regulated by feed-forward and

feedback inhibition. Hypersynchrony likely emerges in the network, leading to very short and sudden bursts of APs instead of paced activity.

When we blocked all excitatory and inhibitory synaptic transmission (Fig. 4, A4–I), we saw that following CCh application, the spontaneous rhythmic bursts of CA2 PN were very similar to what we observed with NBQX and APV with only the

Table 1. Effect of synaptic transmission on carbachol-induced CA2 PN spontaneous activity

Measurement	Control (n = 25) ^a	Excitatory transmission blocked (n = 7) ^b	Inhibitory transmission blocked (n = 6) ^c	Excitatory and inhibitory transmission blocked (n = 6) ^d	Statistics
ACSF- V_M before CCh application (mV)	-75 ± 1.2	-72 ± 3.1	-80 ± 1.9	-70 ± 4.1	$P = 0.054^e$
CCh- V_M (mV)	-64 ± 1.0	-62 ± 2.1	-64 ± 1.5	-57 ± 2.9^f	$P = 0.036^e$
$\Delta_{\text{ACSF-CCh } V_M}$ (mV)	11 ± 1.0	9.5 ± 1.5	16 ± 1.9	13 ± 1.4	$P = 0.065^e$
Depolarization rate (mV/min)	6.5 ± 0.8	9.2 ± 3.4	9.4 ± 2.3	8.6 ± 2.0	$P = 0.52^g$
Burst onset (min)	6.4 ± 0.7	4.6 ± 1.8	4.7 ± 1.2	3.5 ± 0.6	$P = 0.21^e$
Interburst interval (s)	100 ± 14.7	36 ± 8.3^h	113 ± 41.9	36 ± 5.6^h	$P = 0.006^g$
Burst- V_M (mV)	-42 ± 1.0	-36 ± 1.6	-42 ± 2.2	-40 ± 3.2	$P = 0.41^e$
Interburst- V_M (mV)	-62 ± 0.8	-56 ± 1.4^i	-63 ± 1.9	-56 ± 1.1^j	$P < 0.001^e$
$\Delta_{\text{burst-IBI } V_M}$ (mV)	21 ± 1.2	18 ± 2.6	22 ± 3.7	14 ± 2.3	$P = 0.11^e$
Burst rise rate (mV/s)	3.5 ± 0.5	5.9 ± 1.1	59 ± 26^h	3.6 ± 0.6	$P < 0.001^g$
Burst decay rate (mV/s)	-4.6 ± 0.8	-4.3 ± 0.7	-13.7 ± 4.0	-4.8 ± 0.6	$P = 0.087^g$
Burst duration (s)	3.8 ± 0.5	2.6 ± 0.7	1.1 ± 0.3^h	2.4 ± 0.6	$P = 0.037^g$
Number of APs/burst	22 ± 2.5	11 ± 1.8^h	13 ± 2.3	11 ± 2.5^h	$P = 0.008^g$
Firing frequency in burst (Hz)	13 ± 1.9	9.5 ± 1.4	36 ± 7.9^h	9.7 ± 4.5	$P = 0.012^g$

^a10 μM CCh.

^b10 μM CCh, 10 μM NBQX, and 50 μM APV.

^c10 μM CCh, 1 μM SR95531, and 2 μM CGP5584A.

^d10 μM CCh, 10 μM NBQX, 50 μM APV, 1 μM SR95531, and 2 μM CGP5584A.

^eOne-way ANOVA.

^f $P = 0.025$ vs. CT; Tukey post hoc test.

^gKruskal-Wallis test.

^h $P < 0.05$ vs. CT; Dunn-Holland-Wolfe post hoc test.

ⁱ $P = 0.001$ vs. CT; $P = 0.013$ vs. SR; Tukey post hoc test.

^j $P = 0.006$ vs. CT; $P = 0.033$ vs. SR; Tukey post hoc test.

interburst- V_M , interburst intervals and number of APs per burst different from control conditions (Fig. 4, B, D, and G; Table 1). Thus, while the CA2 PN AP bursting activity is shaped by both excitatory and inhibitory synaptic input, the intrinsic conductance of these neurons permits them to undergo rhythmic bursts of AP firing in the presence of 10 μM CCh.

CCh affects transmission onto CA2 PNs

High cholinergic tone has been shown to suppress synaptic transmission in the hippocampus in a laminar-selective way (Hasselmo and Schnell, 1994). These observations form a basis for computational models describing cholinergic modulation of hippocampal networks during learning. As this has never been explored in area CA2, and because we found that synaptic transmission shapes burst firing, we decided to examine how excitatory and inhibitory transmission is altered in this area by recording synaptic responses before and after application of 10 μM CCh.

Our first strategy was to use extracellular field recordings to examine evoked excitatory synaptic transmission in area CA2 at proximal inputs in stratum radiatum as well as distal inputs in (SLM in the presence of GABA receptor blockers (Fig. 5, A and B). We observed that application of 10 μM CCh reduced fEPSP amplitudes at both proximal (Fig. 5, A1–A3) and distal (Fig. 5, B1–B3) inputs. The reduction in fEPSP at stratum radiatum was

larger than that measured in SLM, and this difference was statistically significant ($P = 0.0079$, two-way ANOVA, repeated measure). These results are very similar to what has been observed in areas CA1 (Hasselmo and Schnell, 1994) and CA3 (Kremin and Hasselmo, 2007).

We postulate that the application of 10 μM CCh is likely acting on CA2 PNs via activation of mAChRs. Our finding that application of the M1 and M3 receptor antagonists, pirenzepine and 4-DAMP, prevents the large membrane depolarization, and AP bursting supports this conclusion. However, in the hippocampus, nAChRs have been found to be located at both pre- and postsynaptic compartments and can modulate glutamatergic transmission (McGehee et al., 1995; Halff et al., 2014). To explore a possible contribution of nAChR participation in synaptic transmission in area CA2, we applied 10 μM of the nAChR blocker mecamylamine and measured the resulting CCh-induced decrease in synaptic transmission at stratum radiatum (Fig. 5 A3) and SLM (Fig. 5 B3) inputs. We found that blocking nAChRs had no impact on the CCh-induced reduction in synaptic transmission, indicating that these receptors are likely not contributing to the CCh-induced change in synaptic transmission as it is being measured here.

As shown in Fig. 2 B, application of M1/M3 mAChR antagonists prevented CCh-induced membrane depolarization. To determine

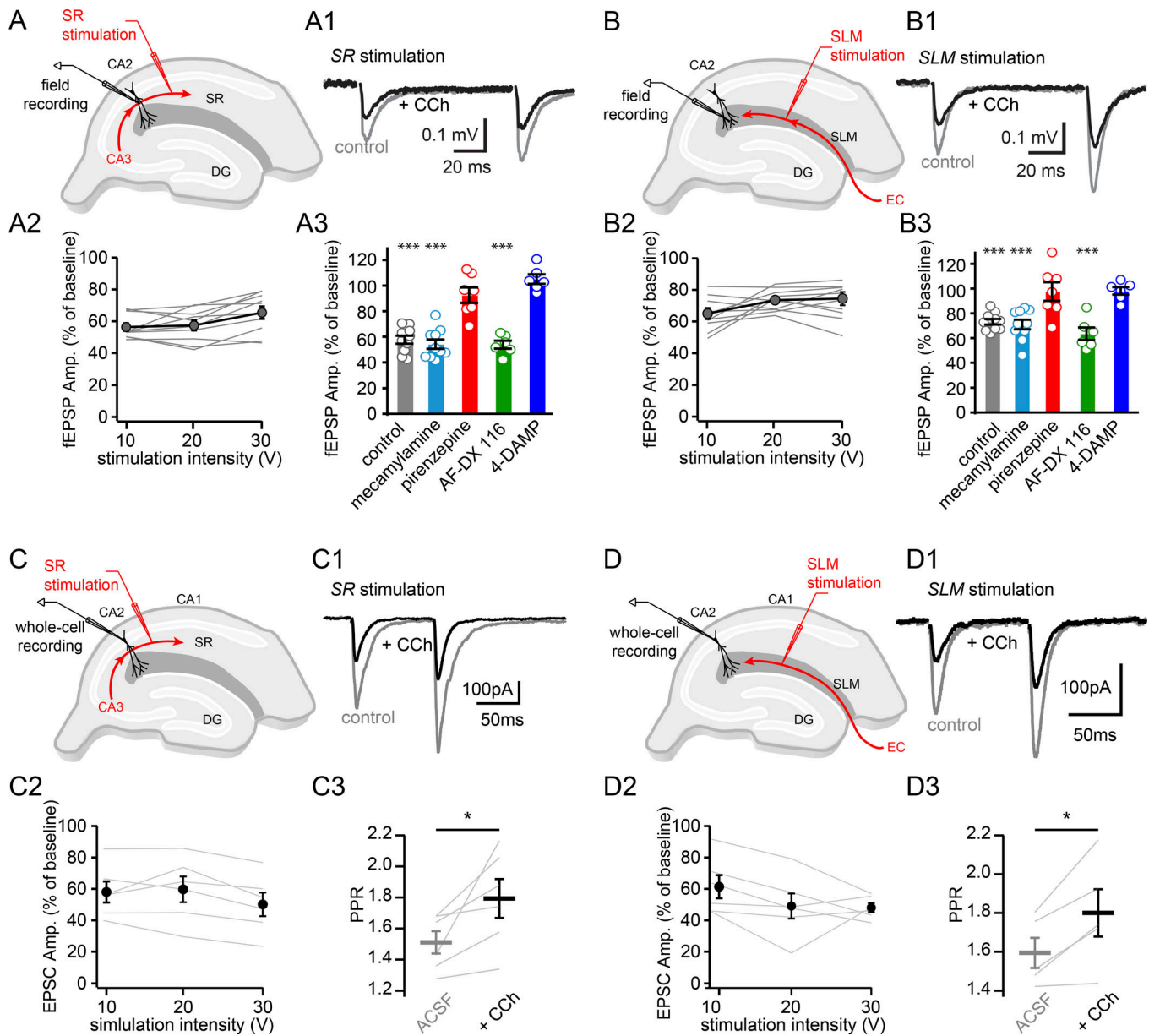


Figure 5. CCh attenuates excitatory synaptic transmission onto CA2 PNs. (A) Diagram illustrating extracellular recording configuration with recording and stimulation electrodes in stratum radiatum. (A1) Sample traces of field responses to electrical stimulation of stratum radiatum input to area CA2 before (gray) and after (black) 10 μ M CCh application in the presence of GABA receptor antagonists (1 μ M SR95531 and 2 μ M CGP5584A). (A2) Summary graph of the proportion of control response amplitude (Amp.) remaining in stratum radiatum after CCh with increasing stimulation intensities ($n = 10$). (A3) Summary graph of the proportion of fEPSP amplitude remaining with 20-V stimulation in stratum radiatum after application of 10 μ M CCh alone (control, gray; $n = 10$, $57.2 \pm 2.5\%$, one-sample t test, $P = 2.8 \times 10^{-7}$) or in the presence of 10 μ M mecamylamine, an nAChR blocker (turquoise; $n = 10$, $54.2 \pm 3.6\%$, one-sample t test, $P = 4.8 \times 10^{-7}$); 10 μ M pirenzepine, an M1 muscarinic receptor blocker (red; $n = 7$, $92.6 \pm 6.0\%$, one-sample t test, $P = 0.26$); 10 μ M AF-DX 116, an M2 muscarinic receptor blocker (green; $n = 6$, $53.8 \pm 3.1\%$, one-sample t test, $P = 2.5 \times 10^{-5}$), and 10 μ M 4-DAMP, an M3 muscarinic receptor blocker (blue; $n = 6$, $105 \pm 3.7\%$, one-sample t test, $P = 0.23$). (B) Diagram illustrating extracellular recording configuration with recording and stimulation electrodes in SLM. (B1) Same as A1, except with SLM input stimulation. (B2) Summary graph of the proportion of control response amplitude remaining in SLM after CCh with increasing stimulation intensities ($n = 10$). (B3) Summary graph of the proportion of fEPSP amplitude remaining with 20-V stimulation in SLM after 10 μ M CCh application (control, gray; $n = 10$, $68.9 \pm 2.2\%$, one-sample t test, $P = 8.8 \times 10^{-7}$) or in the presence of 10 μ M mecamylamine (turquoise; $n = 10$, $70.9 \pm 3.8\%$, one-sample t test, $P = 3.8 \times 10^{-5}$); 10 μ M pirenzepine (red; $n = 7$, $97.7 \pm 7.5\%$, one-sample t test, $P = 0.766$); 10 μ M AF-DX 116 (green; $n = 6$, $63.46 \pm 5.0\%$, one-sample t test, $P = 7.9 \times 10^{-4}$); and 10 μ M 4-DAMP (blue; $n = 6$, $98.2 \pm 3\%$, one-sample t test, $P = 0.567$). (C) Diagram illustrating whole-cell recording configuration from CA2 PNs with stratum radiatum input stimulation in acute hippocampal slices. (C1) Sample traces of evoked EPSC recorded in a CA2 PN held at -70 mV with electrical stimulation of stratum radiatum input before (gray) and after (black) 10 μ M CCh application in the presence of GABA receptor antagonists (1 μ M SR95531 and 2 μ M CGP5584A). (C2) Summary graph of the proportion of control response amplitude remaining after CCh with increasing stimulation intensities in stratum radiatum ($n = 6$; percentage remaining at 20-V stimulation = $57.3 \pm 10.2\%$, one-sample t test, $P = 0.008$). (C3) Paired-pulse ratio at 20-V stimulation ($n = 6$; before CCh, 1.5 ± 0.1 ; after CCh, 1.8 ± 0.1 ; percentage increase = $19 \pm 7\%$, paired t test, $P = 0.041$). (D) Same as C with SLM input stimulation. (D1) Same as in C1 except with SLM input stimulation. (D2) Summary graph of the proportion of control response amplitude remaining after CCh with increasing stimulation intensities in SLM; $n = 6$; percentage remaining at 20-V stimulation = $49.1 \pm 8.0\%$, one-sample t test, $P = 0.001$). (D3) Paired-pulse ratio at 20-V stimulation ($n = 5$; before CCh, 1.6 ± 0.1 ; after CCh, 1.8 ± 0.1 ; percentage increase = $13 \pm 3\%$, paired t test, $P = 0.024$). *, $P < 0.05$; ***, $P < 0.001$.

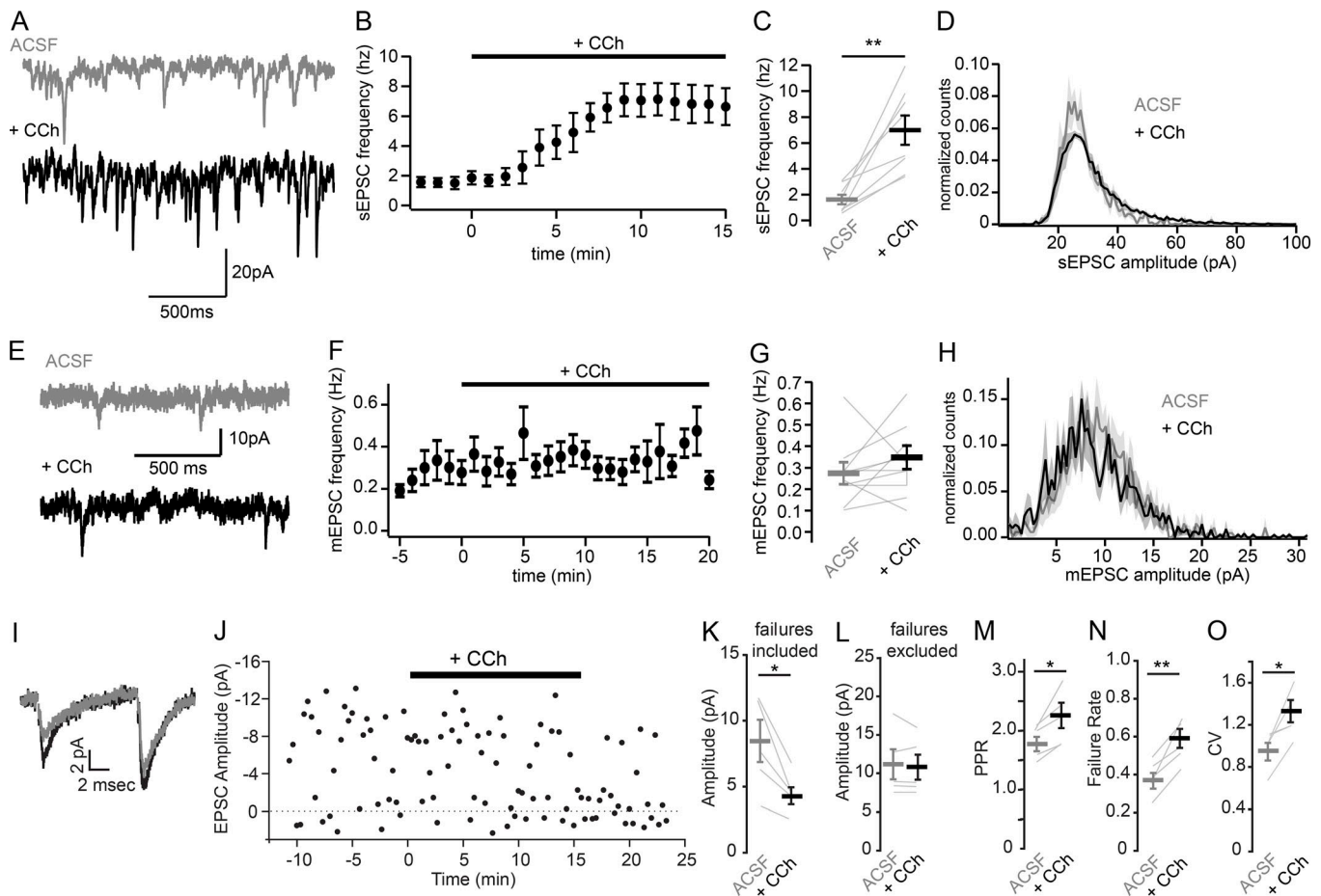


Figure 6. CCh decreases excitatory transmission through a presynaptic mechanism. (A) Sample traces of sEPSCs recorded in whole-cell voltage-clamp configuration from a CA2 PN before (top, gray) and after (bottom, black) application of 10 μ M CCh on acute hippocampal slice. (B) Summary graph of the time course of sEPSC frequency recorded in whole-cell voltage-clamp configuration from CA2 PNs upon 10 μ M CCh wash-in ($n = 8$; error bars represent SEM). (C) Summary graph of the sEPSC frequency recorded in whole-cell voltage-clamp configuration from CA2 PNs before and after 10 μ M CCh application ($n = 8$; before CCh, 1.6 ± 0.4 Hz; after CCh, 7.0 ± 1.1 Hz; paired t test, $P = 0.002$; individual cells shown as thin lines; population averages shown as thick lines; error bars represent SEM). (D) Normalized histograms of the sEPSC amplitude recorded in whole-cell voltage-clamp configuration from CA2 PNs before (gray) and after (black) 10 μ M CCh application ($n = 7$; first peaks in amplitude distributions: before CCh, 25.1 ± 0.6 pA; after CCh, 23.9 ± 1.1 pA; paired t test, $P = 0.27$, shaded areas represent SEM). (E) Sample traces of mEPSCs recorded in the presence of 100 nM TTX and 4 mM CaCl_2 before (top, gray) and after (bottom, black) application of 10 μ M CCh. (F) Summary graph of the time course of mEPSC frequency recorded in voltage-clamp configuration from CA2 PNs upon 10 μ M CCh application ($n = 9$, error bars represent SEM). (G) Summary graph of the mEPSC frequency recorded before and after 10 μ M CCh application ($n = 9$; before CCh, 0.27 ± 0.05 Hz; after CCh, 0.35 ± 0.05 Hz; paired t test, $P = 0.312$; individual cells shown as thin lines; population averages shown as thick lines; error bars represent SEM). (H) Normalized histograms of the mEPSC amplitude recorded before (gray) and after (black) 10 μ M CCh application ($n = 9$; first peaks in amplitude distributions: before CCh, 9.0 ± 0.6 pA; after CCh, 8.6 ± 0.9 pA; paired t test, $P = 0.489$; shaded areas represent SEM). (I) Averaged sample traces of EPSCs evoked with minimal stimulation of CA3 inputs and recorded in CA2 PNs before (black trace) and after (gray trace) 10 μ M CCh application. (J) Example data from a single experiment using minimal stimulation in stratum radiatum to evoke EPSCs in CA2 PNs. Each EPSC amplitude is plotted over time before and during CCh application. (K–O) Summary graphs. (K) EPSC amplitude including failures ($n = 5$; paired t test, $P = 0.023$). (L) The amplitude excluding failures (paired t test, $P = 0.555$). (M) The paired pulse ratio (PPR, paired t test, $P = 0.0241$). (N and O) Failure rate (paired t test, $P = 0.007$; N) and coefficient of variation (paired t test, $P = 0.028$; O) measured before and after 10 μ M CCh application (individual cells shown as thin lines; population averages shown as thick lines; error bars represent SEM). *, $P < 0.05$; **, $P < 0.01$.

if activation of these receptors is also a requirement for the attenuation of synaptic transmission, we performed extracellular recordings of synaptic transmission in the presence of pirenzepine (10 μ M), AF-DX 116 (10 μ M), or 4-DAMP (1 μ M) mAChR blockers. We found that with either the M1 or M3 mAChRs blocked, CCh application had no effect on the amplitude of evoked EPSPs at synapses in both stratum radiatum and SLM (Fig. 5, A3 and B3). These data indicate that M1 and M3 receptors are primarily responsible for mediating the CCh-induced decrease in

fEPSP amplitude. With M2 receptors blocked with AF-DX 116, we observed that the fEPSP amplitude remaining after CCh application was similar to control in both stratum radiatum and SLM.

To better examine the effect of CCh application on synaptic transmission independently from membrane depolarization effects, we performed whole-cell recordings of CA2 PNs with cesium intracellular solution. We voltage clamped the cells at -70 mV and evoked EPSCs from CA2 PNs with stimulating electrodes in stratum radiatum and SLM in the presence of

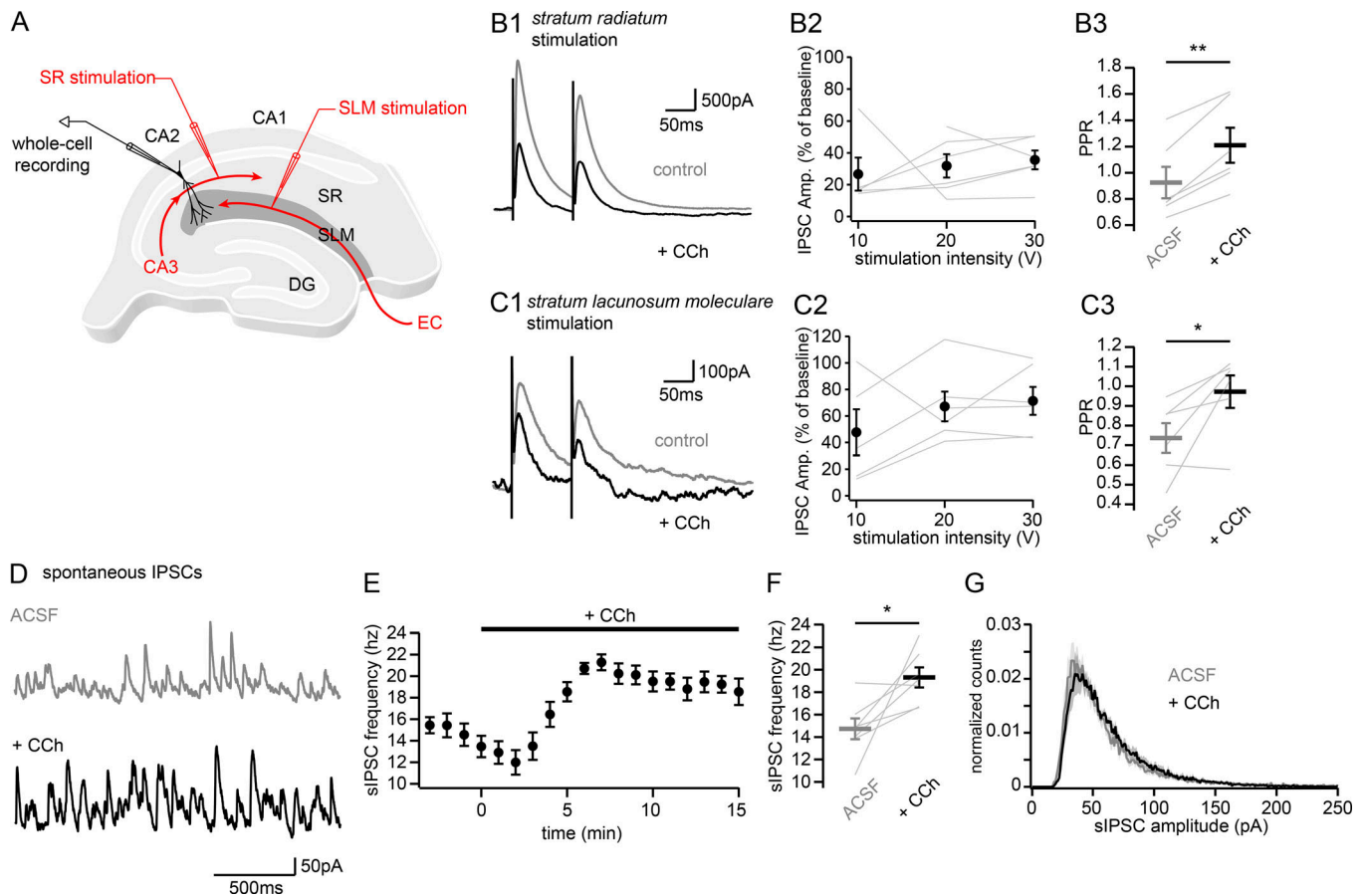


Figure 7. CCh alters inhibitory synaptic transmission onto CA2 PN. (A) Diagram illustrating whole-cell recording configuration from CA2 PN with stratum radiatum and SLM input stimulation in acute hippocampal slices. Recordings were performed at +10 mV with intracellular cesium in the pipette. (B) Sample traces (B1) of evoked IPSCs recorded in a CA2 PN with electrical stimulation of stratum radiatum input before (gray) and after (black) 10 μ M CCh application and summary graphs (B2) of the proportion of control response amplitude remaining after CCh with increasing stimulation intensities ($n = 6$; percentage remaining at 20-V stimulation = $31.9 \pm 7.3\%$, one-sample t test, $P < 0.001$). (B3) Paired-pulse ratio at 20-V stimulation ($n = 6$; before CCh, 0.9 ± 0.1 ; after CCh, 1.2 ± 0.1 ; percentage increase = $32 \pm 5\%$, paired t test, $P = 0.001$). (C) Same as B with SLM input stimulation (C1, sample traces; C2, summary graph; $n = 6$; percentage remaining at 20-V stimulation = $67.1 \pm 11.2\%$, one-sample t test, $P = 0.033$). (C3) Paired-pulse ratio at 20-V stimulation ($n = 6$; before CCh, 0.7 ± 0.1 ; after CCh, 1.0 ± 0.1 ; percentage increase: $39 \pm 19\%$ by CCh; paired t test, $P = 0.045$). (D) Sample traces of sIPSCs recorded in whole-cell voltage-clamp configuration from a CA2 PN before (top, gray) and after (bottom, black) application of 10 μ M CCh on acute hippocampal slices. (E) Summary graph of the time course of sIPSC frequency recorded in whole-cell voltage-clamp configuration from CA2 PN upon 10 μ M CCh wash-in ($n = 7$; error bars represent SEM). (F) Summary graph of the sIPSC frequency recorded in whole-cell voltage-clamp configuration from CA2 PN before and after CCh application ($n = 7$; before CCh, 15 ± 0.9 Hz; after CCh, 19 ± 0.9 Hz, paired t test, $P = 0.026$; individual cells shown as gray lines; population averages shown as thick lines; error bars represent SEM). (G) Normalized histograms of the sIPSC amplitude recorded in whole-cell voltage-clamp configuration from CA2 PN before (gray) and after (black) 10 μ M CCh application ($n = 7$; first peaks in amplitude distributions: before CCh, 36.0 ± 2.0 pA; after CCh, 40.4 ± 2.6 pA; paired t test, $P = 0.29$; shaded areas represent SEM). *, $P < 0.05$; **, $P < 0.01$.

GABA receptor blockers. Consistent with our field recordings, we observed a decrease in EPSC amplitude following CCh application in both stratum radiatum and SLM inputs (Fig. 5, C and D). However, in contrast to the field recordings, this reduction of EPSC amplitude did not significantly differ between stratum radiatum and SLM inputs (t test between proportion of control response in stratum radiatum and SLM, $P = 0.47$). Thus, we conclude that CCh application decreases excitatory transmission in addition to depolarizing CA2 PN. We observed an increase in the paired-pulse ratio of evoked EPSCs in stratum radiatum and SLM (Fig. 5, C3–D3), consistent with a presynaptic effect of CCh on synaptic vesicle release probability.

To determine whether there is also a postsynaptic change in excitatory transmission, we monitored spontaneous EPSCs

(sEPSCs). We found that the sEPSC frequency increased within 5 min following CCh application (Fig. 6, A–C). We hypothesize that this increase in frequency results from enhanced network activity, as connected synaptic inputs will be undergoing spontaneous bursts of AP firing. We did not observe a change in the amplitude of individual synaptic events (Fig. 6 D), consistent with the hypothesis that CCh did not act postsynaptically to reduce synaptic transmission. To further confirm the presynaptic action of CCh and decouple the network activity from synaptic transmission, we performed this experiment in the presence of 100 nM TTX and 4 mM extracellular CaCl_2 , permitting us to record mEPSCs. We did not detect a change in mEPSC frequency before and after application of CCh (Fig. 6, E–G). Furthermore, we observed no change in mEPSC quantal

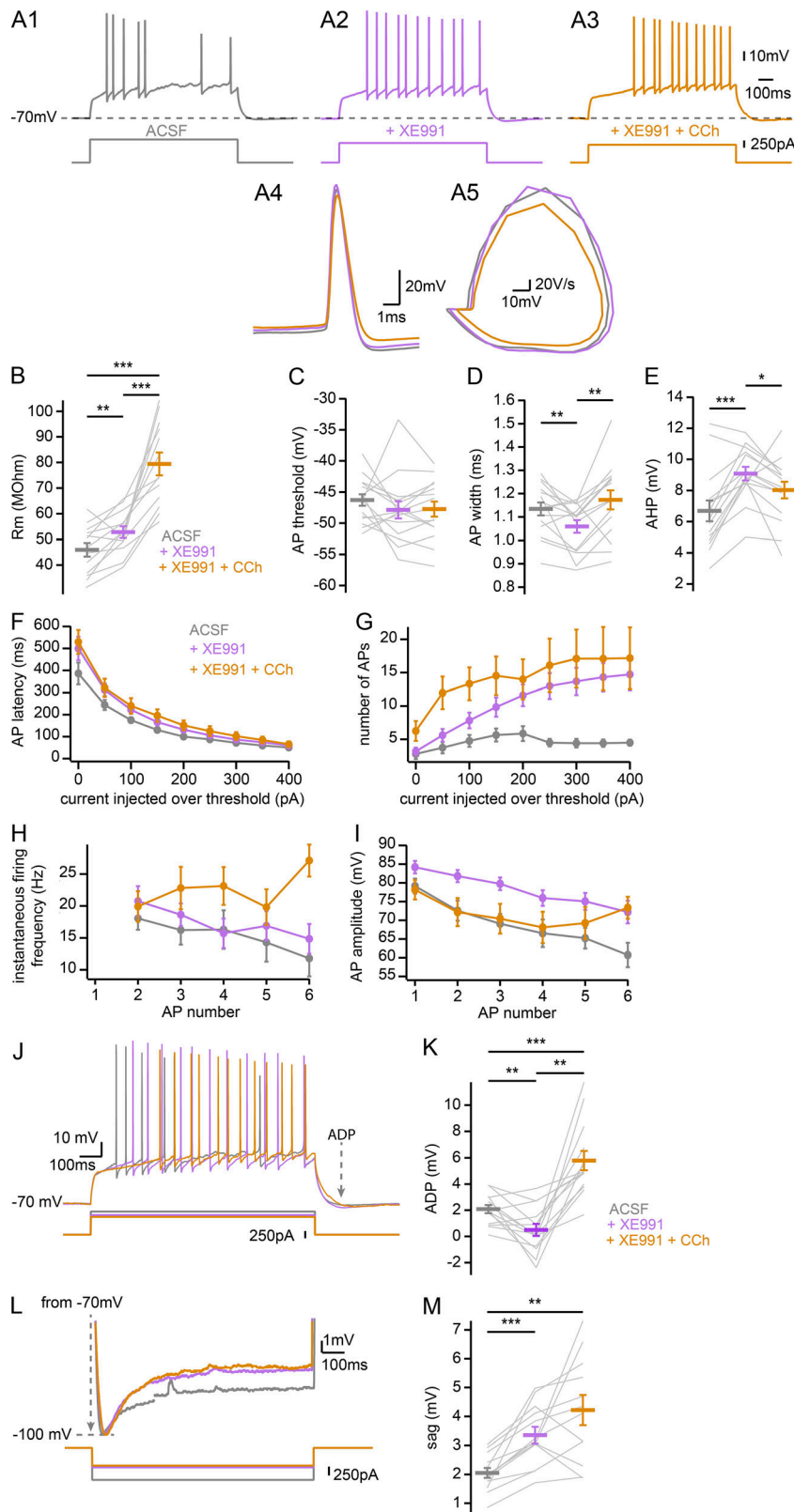


Figure 8. Contribution of the M-current to CCh effects on CA2 PN intrinsic properties. (A) Sample traces of AP firing in response to depolarizing current step injections recorded in whole-cell current-clamp configuration from a CA2 PN in control (A1, gray), 10 μM XE-991 (A2, purple), and 10 μM XE-991 and 10 μM CCh (A3, orange), expanded view of the first AP in each condition (A4); and corresponding phase plane plot (A5). (B–I) Summary graphs of CA2 PNs AP firing properties in control (gray), 10 μM XE-991 (purple), and 10 μM XE-991 and 10 μM CCh (orange; *n* = 15; individual cells shown as thin lines; population averages shown as thick lines; error bars represent SEM). (B) *R_m* (before XE-991, 46 ± 2.6 MOhm; after XE-991, 53 ± 2.3 MOhm; after XE-991 and CCh = 79 ± 4.5 MOhm; Friedman ANOVA, *P* < 0.001). (C) AP threshold (before XE-991, -46.3 ± 0.9 mV; after XE-991, -47.9 ± 1.4 mV; after XE-991 and CCh, -47.7 ± 1.2 mV; Friedman ANOVA, *P* = 0.37). (D) AP width at half-maximal amplitude (before XE-991, 1.13 ± 0.03 ms; after XE-991, 1.06 ± 0.03 ms; after XE-991 and CCh, 1.17 ± 0.04 ms; repeated-measures ANOVA, *P* = 0.002). (E) AHP (before XE-991, 6.7 ± 0.7 mV; after XE-991, 9.1 ± 0.4 mV; after XE-991 and CCh, 8.0 ± 0.5 mV; repeated-measures ANOVA, *P* < 0.001). (F) Latency to fire first AP per current step as a function of current injection over rheobase (200 pA over rheobase: before XE-991, 100 ± 7.6 ms; after XE-991, 132 ± 14.0 ms; after XE-991 and CCh, 147 ± 19.7 ms; Friedman ANOVA, *P* = 0.006). (G) Number of APs fired per current step as a function of current injection over rheobase (200 pA over rheobase, before XE-991, 6 ± 1; after XE-991, 12 ± 2; after XE-991 and CCh, 15 ± 3; Friedman ANOVA, *P* = 0.27). (H) Instantaneous firing frequency of APs as a function of AP number during a current step of intensity chosen 1.5 times above rheobase (first couple of APs frequency, before XE-991, 18 ± 1.8 Hz; after XE-991, 20 ± 2.3 Hz; after XE-991 and CCh, 20 ± 2.4 Hz; repeated-measures ANOVA, *P* = 0.55). (I) AP amplitude as a function of AP number during a current step of intensity chosen 1.5 times above rheobase (first AP amplitude, before XE-991, 79 ± 2.0 mV; after XE-991, 84 ± 1.6 mV; after XE-991 and CCh, 78 ± 2.6 mV; repeated-measures ANOVA on first AP amplitude, *P* = 0.044). (J) Sample traces of the ADP following a depolarizing current step injection in a CA2 PN recorded in whole-cell current-clamp configuration in control (gray), 10 μM XE-991 (purple), and 10 μM XE-991 and 10 μM CCh (orange). (K) Summary graph of CA2 PNs ADP in control (gray), 10 μM XE-991 (purple), and 10 μM XE-991 and 10 μM CCh (orange; *n* = 14, before XE-991, 2.1 ± 0.3 mV; after XE-991, 0.5 ± 0.5 mV; after XE-991 and CCh, 5.8 ± 0.7 mV; Friedman ANOVA, *P* < 0.001; individual cells shown as thin lines; population averages shown as thick lines; error bars represent SEM). (L) Sample traces of voltage sag in response to hyperpolarizing current step injections recorded in whole-cell current-clamp configuration from a CA2 PN in control (gray), 10 μM XE-991 (purple), and 10 μM XE-991 and 10 μM CCh (orange). (M) Summary graphs of CA2 PN voltage sag following hyperpolarization to -100 mV in control (gray), 10 μM XE-991 (purple), and 10 μM XE-991 and 10 μM CCh (orange; *n* = 12, preXE991, 2.1 ± 0.2 mV; after XE-991, 3.5 ± 0.3 mV; after XE-991 and CCh, 4.2 ± 0.5 mV; Friedman ANOVA, *P* < 0.001; individual cells shown as gray lines; population averages shown as thick lines; error bars represent SEM). *, *P* < 0.05; **, *P* < 0.01; ***, *P* < 0.001.

Downloaded from https://rpress.org/jgp/article-pdf/152/4/6201912462/1041504/jgp_201912462.pdf by INSERM user on 04 June 2020

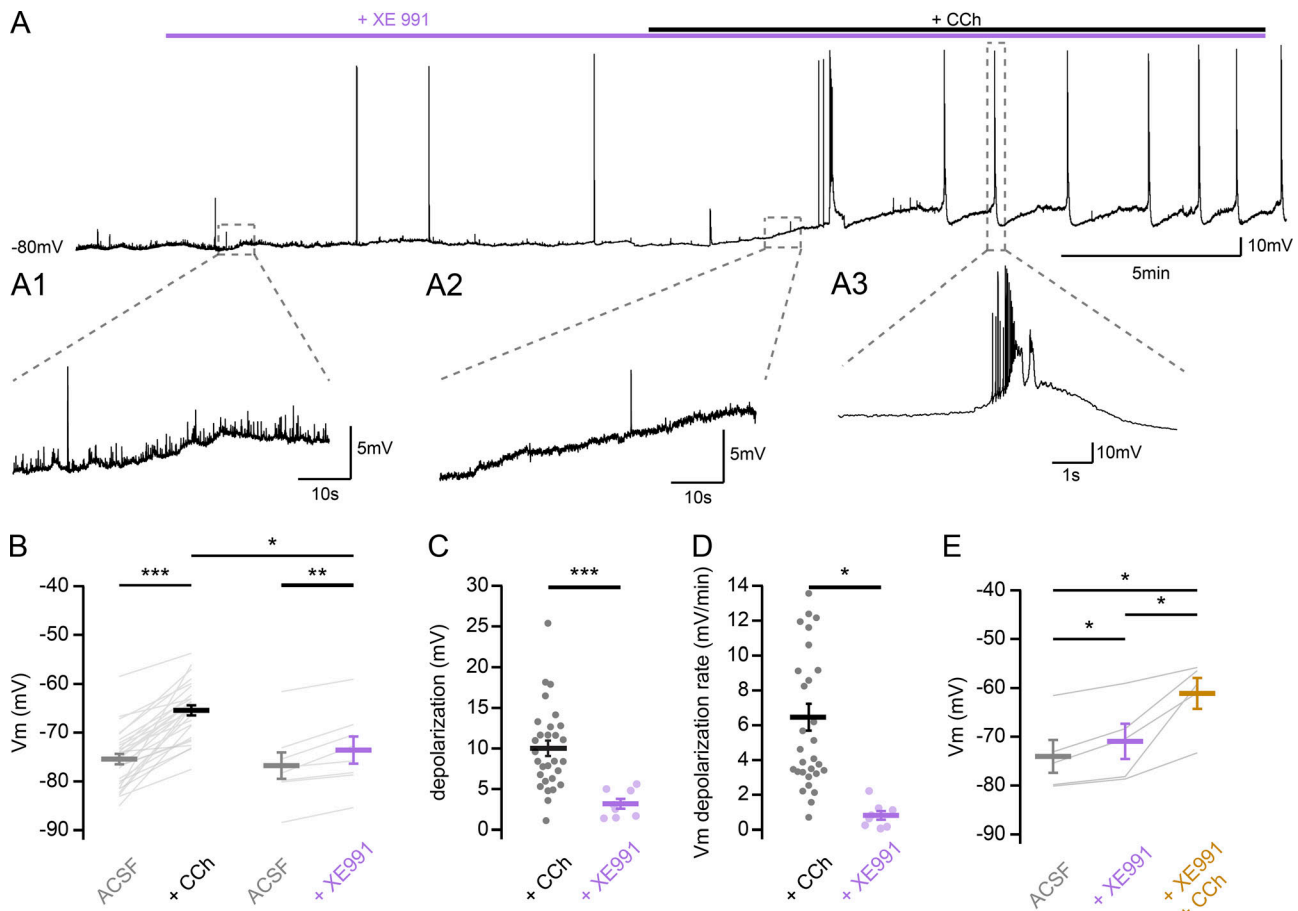


Figure 9. Reduction of the M-current alone does not underlie the CCh-induced AP bursting in CA2 PN. (A) Sample trace recorded in whole-cell current-clamp configuration from a CA2 PN and expanded views showing only minimal V_M depolarization without bursts during application of 10 μ M of the M-current blocker XE-991 (A1) followed by increased depolarization (A2) and bursts (A3) upon subsequent application of 10 μ M CCh in acute hippocampal slice. (B–D) Summary graphs of CA2 PN V_M changes with application of 10 μ M CCh (black, $n = 29$; same CCh data shown in Fig. 8, C and D, as 10 μ M CCh in Fig. 2, E and F, respectively) or 10 μ M XE-991 (purple, $n = 8$; individual cells shown as dots; population averages shown as thick lines; error bars represent SEM). (B) V_M levels at resting and after the initial depolarization induced by CCh or XE-991 (before CCh, -75.4 ± 1.1 ; after CCh, -65.4 ± 1.0 ; before XE-991, -76.7 ± 2.7 mV; after XE-991, -73.6 ± 2.8 mV; paired t test before CCh and after CCh, $P < 0.001$; paired t test before XE-991 and after XE-991, $P = 0.001$; t test before CCh and before XE-991, $P = 0.65$; t test after CCh and after XE-991, $P = 0.023$). (C) V_M initial depolarization magnitude upon CCh or XE-991 application (CCh, 10.0 ± 0.9 mV; XE-991, 3.2 ± 0.6 mV; Mann–Whitney U test, $P < 0.001$). (D) V_M initial depolarization rate upon CCh or XE-991 application (CCh, 6.0 ± 0.7 mV/min; XE-991, 0.8 ± 0.3 mV/min; Mann–Whitney U test, $P < 0.001$). (E) V_M levels following sequential addition of XE-991 and XE-991 plus CCh (before XE-991, -74.0 ± 3.4 mV; after XE-991, -70.9 ± 3.6 mV; after XE-991 and CCh, -61.1 ± 3.2 mV; repeated-measures ANOVA, $P = 0.001$, $n = 5$). *, $P < 0.05$; **, $P < 0.01$; ***, $P < 0.001$.

size (Fig. 6 H), consistent with a lack of postsynaptic effect of CCh. While these results support the hypothesis that CCh is acting presynaptically to reduce EPSC amplitude, the addition of TTX prevented >90% of spontaneous synaptic events, resulting in a very low mEPSC frequency. While this value is very similar to what has recently been reported by others for area CA2 (Modi et al., 2019), this low event frequency may be problematic in detecting changes in release probability. Furthermore, these spontaneous events are not input specific. Thus, we used a third method to investigate a potential presynaptic site of action of CCh, performing minimal stimulation of stratum radiatum inputs while recording CA2 PN before and after CCh application (Fig. 6, I and J). We observed that the amplitude of synaptic events decreased when failures were included (Fig. 6 K) but was not changed when failures were excluded (Fig. 6 L). Consistently, when the amplitudes of the first and second stimulation

were averaged with failures included, CCh application resulted in an increase in the paired pulse ratio (Fig. 6 M), indicating that release probability is decreased with CCh. Likewise, following CCh application, we observed an increase in failure rate (Fig. 6 N) as well as in the coefficient of variation (Fig. 6 O), consistent with a decrease in release probability.

We examined inhibitory transmission in area CA2 by using the same voltage clamp approach but held the CA2 PN at +10 mV in the absence of GABA blockers. We observed that CCh application reduced inhibitory postsynaptic current (IPSC) amplitudes evoked by both stratum radiatum and SLM input stimulation (Fig. 7, A–C). This reduction of IPSC amplitude was largest in stratum radiatum compared with SLM (t test between proportion of control response in stratum radiatum and SLM, $P = 0.028$). Paired-pulse ratios of evoked IPSCs in stratum radiatum and SLM were also increased after CCh application

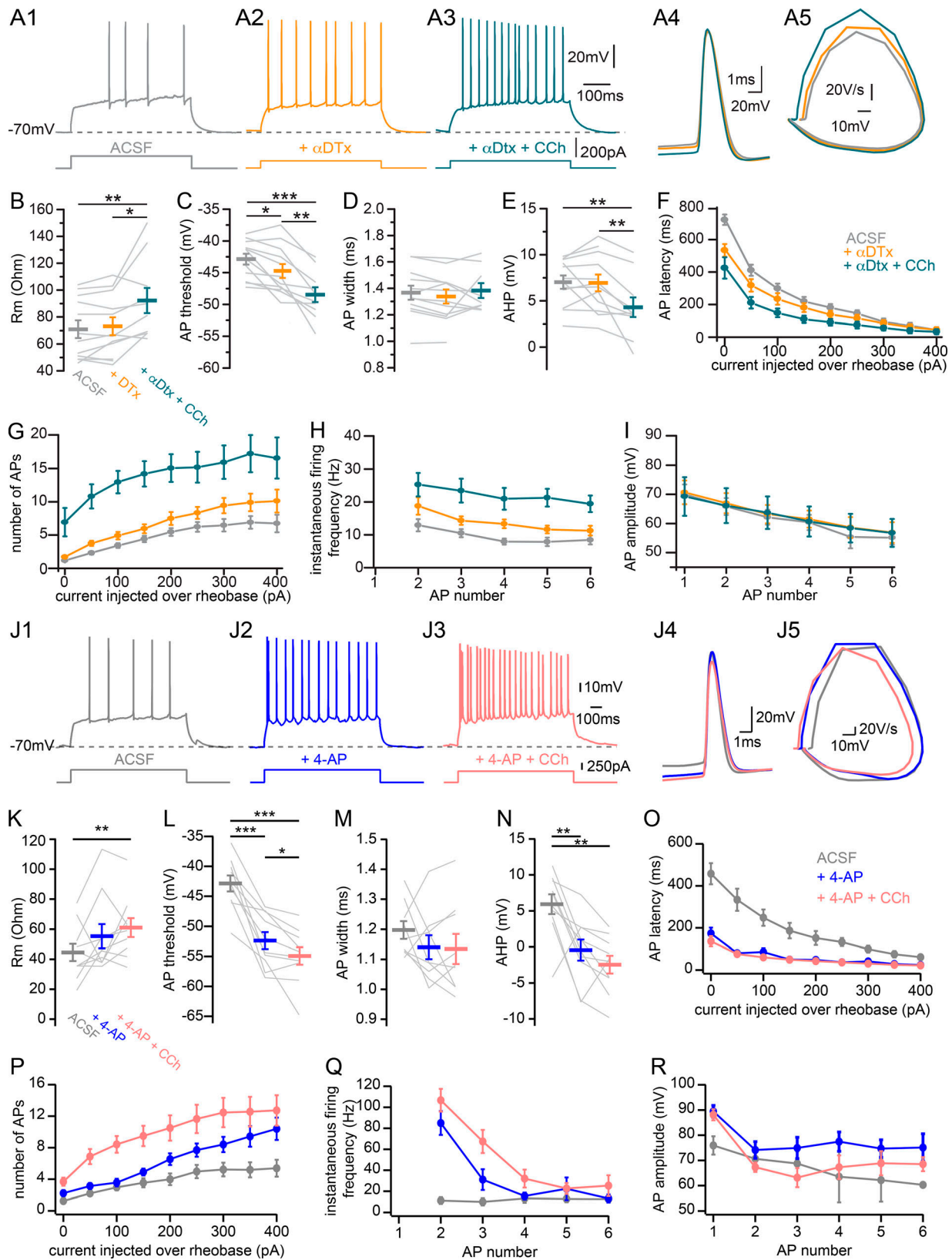


Figure 10. **Contribution of voltage-activated potassium currents to CCh-induced effects on CA2 PN intrinsic properties.** (A) Sample traces of AP firing in response to depolarizing current step injections recorded in whole-cell current-clamp configuration from a CA2 PN in control ACSF (A1, gray), 100 nM α -DTX (A2, orange), and 100 nM α -DTX and 10 μ M CCh (A3, green); expanded view of the first AP in each condition (A4); and corresponding phase plane plot (A5). (B–I) Summary graphs of CA2 PNs AP firing properties in control (gray), 100 nM α -DTX (orange), and 100 nM α -DTX and 10 μ M CCh (green; $n = 12$ for before and after α -DTX, $n = 9$ for after α -DTX and CCh); individual cells shown as thin lines; population averages shown as thick lines; error bars represent SEM). (B) R_m

(before α -DTX, 70.9 ± 6.5 MOhm; after α -DTX, 73.1 ± 6.6 MOhm; after α -DTX and CCh, 92.2 ± 9.4 MOhm; repeated-measures ANOVA, $P = 0.0028$). **(C)** AP threshold (before α -DTX, -42.9 ± 0.8 mV; after α -DTX, -44.7 ± 1.1 mV; after α -DTX and CCh, -48.5 ± 1.1 mV; repeated-measures ANOVA, $P < 0.001$). **(D)** AP width at half-maximal amplitude (before α -DTX, 1.36 ± 0.05 ms; after α -DTX, 1.34 ± 0.05 ms; after α -DTX and CCh, 1.38 ± 0.05 ms; repeated-measures ANOVA, $P = 0.71$). **(E)** AHP (before α -DTX, 7.0 ± 0.7 mV; after α -DTX, 6.9 ± 0.9 mV; after α -DTX and CCh, -4.3 ± 1.1 mV, repeated-measures ANOVA, $P = 0.0021$). **(F)** Latency to fire first AP per current step as a function of current injection over rheobase (200 pA over rheobase, before α -DTX, 180.5 ± 22.5 ms; after α -DTX, 138.1 ± 23.1 ms; after α -DTX and CCh, 91.0 ± 20.3 ms; repeated-measures ANOVA, $P = 0.0016$). **(G)** Number of APs fired per current step as a function of current injection over rheobase (200 pA over rheobase, before α -DTX, 5.5 ± 0.6 ; after α -DTX, 7.5 ± 1.0 ; after α -DTX and CCh, 15.1 ± 2.1 ; Friedman ANOVA, $P < 0.001$). **(H)** Instantaneous firing frequency of APs as a function of AP number during a current step of intensity chosen 1.5 times above rheobase (first couple of APs: before α -DTX, 12.9 ± 1.8 Hz; after α -DTX, 18.7 ± 2.6 Hz; after α -DTX and CCh, 25.3 ± 3.6 Hz; repeated-measures ANOVA, $P < 0.001$). **(I)** AP amplitude as a function of AP number during a current step of intensity chosen 1.5 times above rheobase (first AP: before α -DTX, 70.0 ± 3.4 mV; after α -DTX, 70.7 ± 4.1 mV; after α -DTX and CCh, 69.3 ± 6.6 mV; repeated-measures ANOVA, $P = 0.59$). **(J)** Sample traces of AP firing in response to depolarizing current step injections recorded in whole-cell current-clamp configuration from a CA2 PN in control ACSF (J1, gray), 100 μ M 4-AP (J2, blue), and 100 μ M 4-AP and 10 μ M CCh (J3, pink); expanded view of the first AP in each condition (J4); and corresponding phase plane plot (J5). **(K–R)** Summary graphs of CA2 PNs AP firing properties in control (gray), 100 μ M 4-AP (blue), and 100 μ M 4-AP and 10 μ M CCh (pink; $n = 10$; individual cells shown as thin lines; population averages shown as thick lines; error bars represent SEM). **(K)** R_M (before 4-AP, 44.6 ± 5.7 MOhm; after 4-AP, 55.3 ± 8.0 MOhm; after 4-AP and CCh, 61.0 ± 6.3 MOhm; repeated-measures ANOVA, $P = 0.029$). **(L)** AP threshold (before 4-AP, -42.8 ± 1.3 mV; after 4-AP, -52.4 ± 1.4 mV; after 4-AP and CCh, -54.9 ± 1.5 mV; repeated-measures ANOVA, $P < 0.001$). **(M)** AP width at half-maximal amplitude (before 4-AP, 1.2 ± 0.03 ms; after 4-AP, 1.1 ± 0.04 ms; after 4-AP and CCh, 1.1 ± 0.05 ms; repeated-measures ANOVA, $P = 0.27$). **(N)** AHP (before 4-AP, 5.9 ± 1.4 mV; after 4-AP, -0.4 ± 1.4 mV; after 4-AP and CCh, -2.5 ± 1.2 mV; repeated-measures ANOVA, $P < 0.001$). **(O)** Latency to fire first AP per current step as a function of current injection over rheobase (200 pA over rheobase, before 4-AP, 152 ± 33.9 ms; after 4-AP, 48 ± 5.1 ms; after 4-AP and CCh, 43 ± 3.5 ms; Friedman ANOVA, $P = 0.018$). **(P)** Number of APs fired per current step as a function of current injection over rheobase (200 pA over rheobase, before 4-AP, 4.0 ± 0.7 ; after 4-AP, 6.5 ± 0.7 ; after 4-AP and CCh, 10.5 ± 1.6 ; Friedman ANOVA, $P < 0.001$). **(Q)** Instantaneous firing frequency of APs as a function of AP number during a current step of intensity chosen 1.5 times above rheobase (first couple of APs, before 4-AP, 11.3 ± 3.1 Hz; after 4-AP, 84.9 ± 11.3 Hz; after 4-AP and CCh, 106.7 ± 10.9 Hz; Friedman ANOVA, $P < 0.001$). **(R)** AP amplitude as a function of AP number during a current step of intensity chosen 1.5 times above rheobase (first AP, before 4-AP, 76 ± 3.6 mV; after 4-AP, 89 ± 2.4 mV; after 4-AP and CCh, 88 ± 2.2 mV; repeated-measures ANOVA, $P < 0.001$). *, $P < 0.05$; **, $P < 0.01$; ***, $P < 0.001$.

(Fig. 7, B3–C3). We then gauged how inhibitory transmission was affected by CCh by recording spontaneous IPSCs (sIPSCs). Monitoring sIPSCs by holding CA2 PNs at a potential of +10 mV showed that CCh application increased the sIPSC frequency within 5 min (Fig. 7, D–F). However, the sIPSC amplitude distribution was not changed by CCh (Fig. 7 G), indicating that CCh acts presynaptically to reduce inhibitory transmission by decreasing the probability of GABA release. Altogether, these results show a drastic influence of CCh over synaptic transmission in area CA2.

Contribution of M-current to CCh-induced depolarization

Because CA2 PNs can fire bursts of APs in the absence of synaptic transmission, we examined which ionic conductance underlies the depolarization and spontaneous AP bursting in the presence of CCh. K_{V7} channels, which underlie the M-current, have been shown to be modulated by acetylcholine and play a central role in controlling resting V_M and repetitive and burst firing in CA3 and CA1 PNs (Cobb et al., 1999; Hönigspenger et al., 2015). We hypothesize that this current may play a similar role in CA2 PNs. To test this, we looked at the effect of blocking the M-current with 10 μ M XE-991 on CA2 PN intrinsic properties (Fig. 8 A). For these experiments, care was taken to inject DC as needed to keep the initial V_M at -70 mV. Data were acquired after 20 min of bath application of XE-991. We confirmed that the drug was active by performing whole-cell recordings in area CA1 and reproducing previously published changes in EPSP summation and intrinsic properties (Hönigspenger et al., 2015). First, we examined the effects of XE-991 on CA2 PN intrinsic excitability. Consistent with previous observations that M-current channels are open at rest in CA2 PNs (Tirko et al., 2018), we observed an increase of R_M in CA2 PNs following XE-991 application, with subsequent application of CCh causing further R_M increase (Fig. 8 B). Application of X-991 did not

change AP threshold (Fig. 8 C) but did reduce AP width (Fig. 8 D) and increased AHP (Fig. 8 E). These effects were unchanged or attenuated by further application of CCh (Fig. 8, C–E). Application of XE-991 increased the latency of AP onset (Fig. 8 F) as well as the number of APs per step, albeit only at current injections well above threshold (Fig. 8 G), and occluded the effects of CCh application of these measurements. The milder effect of XE-991 alone compared with XE-991 plus CCh on AP number at low current injections indicates that CCh increases CA2 PN excitability by acting on additional conductances beside the M-current. Although the instantaneous firing frequency tended to be higher and to increase with AP number in XE-991 with CCh, no significant effects were seen in this dataset (Fig. 8 H). XE-991 application alone significantly increased AP amplitude, and addition of CCh reversed that effect, suggesting an M-current-independent effect of CCh in reducing spike amplitude (Fig. 8 I). The ADP following current step termination was reduced in XE-991 compared with ACSF, and subsequent application of CCh led to a further increase (Fig. 8, J and K). Application of XE-991 led to an increase in sag potential (Fig. 8 L). Our explanation of this finding is as follows. Block of the M-current results in a depolarization of the membrane, strongly supporting the conclusion that a fraction of these channels is open at resting V_M . In normal ACSF, the sag current is a result of two processes: the opening of HCN channels, resulting in I_h , and the closing of the K_{V7} channels, resulting in a reduction of M-current. In our protocol, we inject DC to keep the initial starting V_M at -70 mV. We then inject the necessary amount of current to bring the V_M to -100 mV. The reversal potential for potassium is more than -100 mV, so any M-current will be expected to be depolarizing and counteract the nonselective I_h . Thus, in the presence of XE-991, the M-current at rest is blocked, and the step to -100 mV only activates I_h , which appears larger, because it is not attenuated by the closing M-current. Presented differently, the R_M will be higher with XE-991 present, allowing a greater

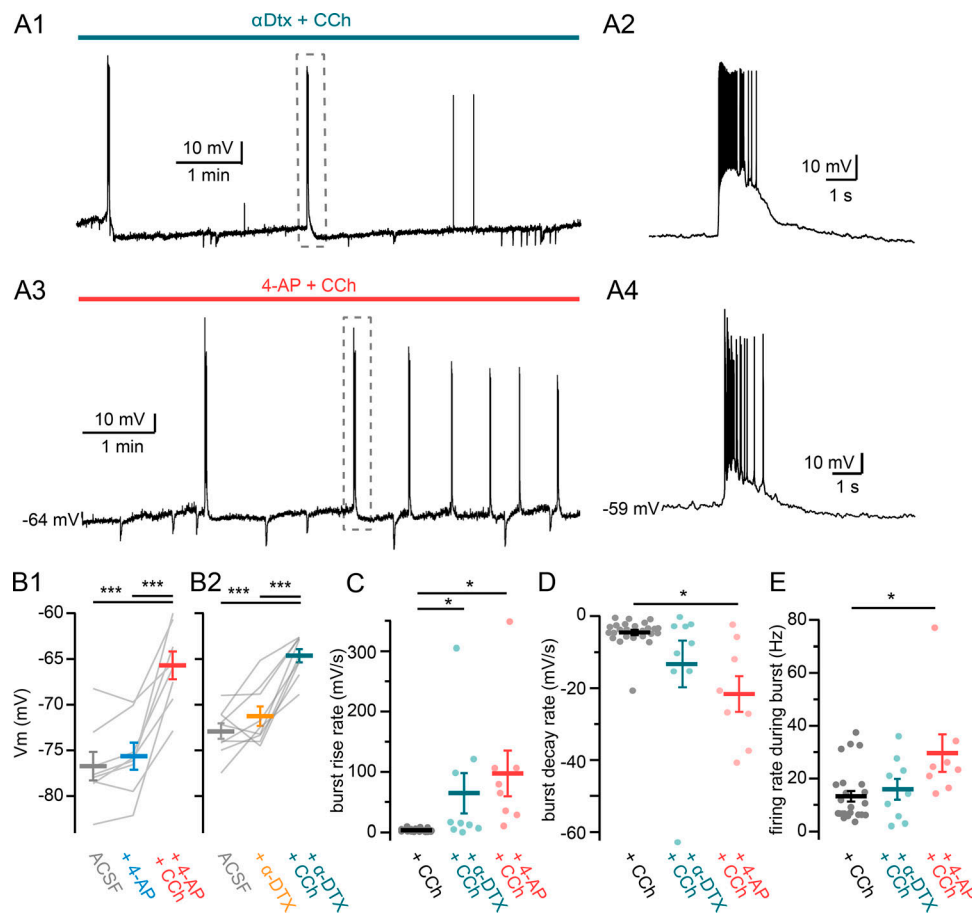


Figure 11. Voltage-gated potassium channels pace AP firing during CCh-induced bursts in CA2 PNs. (A1 and A2) Sample trace of bursts recorded in whole-cell current-clamp configuration from a CA2 PN (A1) and expanded view of a burst (A2) upon application of 10 μM CCh in acute hippocampal slice with D-type potassium channels blocked by application of 100 nM α-DTX. (A3 and A4) Sample trace of bursts (A3) and an expanded view (A4) recorded in the same configuration, except with the nonselective K_V channel blocker 4-AP applied at 100 μM with 10 μM CCh. (B1) V_M levels at rest (gray) after application of 100 μM 4-AP (blue) and after further application of 10 μM CCh (pink; before 4-AP, -76.7 ± 1.6 mV; after 4-AP, -75.6 ± 1.5 mV; after 4-AP and CCh, -65.7 ± 1.5 mV; n = 10; repeated-measures ANOVA, P < 0.001). (B2) V_M levels at rest (gray) and after application of α-DTX (orange) and further application of CCh (green; before α-DTX, -72.9 ± 0.8 mV; after α-DTX, -71.3 ± 1.1 mV; after α-DTX and CCh, -64.7 ± 0.7 mV; n = 10; repeated-measures ANOVA, P < 0.001). (C-E) Summary graphs of burst characteristics with application of 10 μM CCh in control (black, n = 25; same CCh data shown in Fig. 12, C-E, as CCh in Fig. 4, H, I, and E, respectively), 100 nM α-DTX (green, n = 9), and 100 μM 4-AP (pink, n = 8; individual cells shown as dots; population averages shown as thick lines; error bars represent SEM). (C) Burst rise rate (Kruskal-Wallis test, P < 0.001). (D) Burst decay rate (Kruskal-Wallis test, P = 0.008). (E) Firing rate during burst (Kruskal-Wallis test, P = 0.027). *, P < 0.05; ***, P < 0.001.

current at -100 mV, thus making the “sag” measurement larger. Further application of CCh in the presence of XE-991 resulted in similar levels of sag potential (Fig. 8 M). Altogether, these data show that the application of the K_V7 blocker XE-991 partially recapitulated and/or occluded many of the effects of CCh on CA2 PN intrinsic properties, including AHP amplitude, number of APs per current step, and sag current. This suggests a contribution of M-current closing to the effects of CCh on CA2 PN V_M.

During these experiments, we also investigated the consequences of M-current block by XE-991 on CA2 PN V_M by performing current-clamp recordings without injection of DC. We found that application of XE-991 led to a significant depolarization of CA2 PNs. This depolarization was insufficient to elicit AP bursting, and subsequent application of CCh brought further depolarization and AP bursting (Fig. 9 A). XE-991 has been found to be a voltage-dependent blocker of K_V7.2 channels

exogenously expressed in Chinese hamster ovary cells (Greene et al., 2017). Thus, we performed several experiments in which DC was injected to just below threshold to increase the probability of channel block. No difference was observed in the V_M following this manipulation. When compared with CCh-induced initial V_M depolarization of CA2 PNs, the XE-991 effect was smaller and did not bring V_M to depolarized levels sufficient to AP bursting (Fig. 9, B-D). To confirm this, we analyzed the changes in V_M before addition of XE-991, during and following the addition of CCh with XE-991 (Fig. 9 E). With this, we consistently observed an increase in the R_M following XE-991 application, indicating that a proportion of these channels are open at rest (Fig. 8 B). Therefore, this result shows that the M-current is likely open at rest in CA2 PNs, and blocking it leads to a partial depolarization of 3.2 ± 0.6 mV (n = 8). However, addition of CCh resulted in a further increase of R_M, indicating a separate conductance contributing to membrane depolarization, and that

Table 2. Effect of 4-AP and α -DTX on charbachol-induced CA2 PN spontaneous activity

Measurement	Control (n = 25)	Nonselective block of voltage-gated potassium channels (100 μ M 4-AP; n = 8)	D-type potassium channels blocked (100 nM α -DTX; n = 9)	Statistics
ACSF- V_M (mV)	-75 ± 1.2	-76 ± 1.5	-71 ± 1.1	$P = 0.152^a$
CCh- V_M (mV)	-64 ± 1.0	-66 ± 1.5	-65 ± 0.7	$P = 0.613$
$\Delta_{\text{ACSF-CCh}} V_M$ (mV)	11 ± 1.0	10 ± 1.5	7 ± 0.9	$P = 0.058$
Depolarization rate (mV/min)	6.5 ± 0.8	5.4 ± 0.8	3.4 ± 0.6	$P = 0.091$
Burst onset (min)	6.4 ± 0.7	4.4 ± 1.0	6.1 ± 0.9	$P = 0.078^a$
Interburst interval (s)	100 ± 14.7	119 ± 26.2	136 ± 33.0	$P = 0.512^a$
Burst- V_M (mV)	-42 ± 1.0	-37 ± 3.2	-44 ± 0.9	$P = 0.067$
Interburst- V_M (mV)	-62 ± 0.8	-66 ± 1.5	-64 ± 1.2	$P = 0.079^a$
$\Delta_{\text{burst-IBI}} V_M$ (mV)	22 ± 1.3	29 ± 3.2^b	20 ± 1.8	$P = 0.034^a$
Burst rise rate (mV/s)	3.5 ± 0.5	97.5 ± 38.0^c	65.6 ± 33.4^c	$P < 0.001$
Burst decay rate (mV/s)	-4.6 ± 0.8	-21.6 ± 5.0^c	-13.3 ± 6.5	$P = 0.008$
Burst duration (s)	3.8 ± 0.5	1.9 ± 0.7	6.2 ± 1.9	$P = 0.070$
Number of APs/burst	22 ± 2.5	25 ± 7.7	54 ± 19.9	$P = 0.266$
Firing frequency in burst (Hz)	13 ± 1.9	30 ± 7.1^c	16 ± 3.9	$P = 0.027$

^aOne-way ANOVA.

^b $P = 0.046$ vs. CT; Tukey post hoc test.

^c $P < 0.05$ vs. CT; Dunn-Holland-Wolfe post hoc test.

M-current block alone is not sufficient to elicit bursts of AP firing in CA2 PNs in our experiments.

CA2 PN AP firing and CCh-induced bursting are paced by D-type potassium currents

D-type potassium currents have been shown to regulate AP timing and synchrony in hippocampal PNs (Storm, 1988; Cudmore et al., 2010). It may be possible that this current also participates in CCh-induced effect of AP bursting in CA2 pyramidal cells, as CCh application induces a delay in AP firing with current step injection. Furthermore, activation of M1 and M3 muscarinic receptors can result in depletion of phosphatidylinositol 4,5-bisphosphate (PIP₂) in hippocampal PNs (Hackelberg and Oliver, 2018). This results in decreased M-current, but also potentially an increase in K_v1.2 current (Rodríguez-Menchaca et al., 2012). To examine this further, we blocked D-type potassium currents with 100 nM α -DTX, a compound that specifically blocks K_v1.1, 1.2, and 1.6 voltage-gated ion channels. We then injected current steps to measure CA2 PN AP firing properties before and after the application of CCh to determine the contribution of this family of ion channels to mAChR-induced changes in intrinsic properties.

First, we assessed the role of D-type potassium currents on CA2 PN intrinsic properties and their contribution to CCh-induced changes by recording in whole-cell mode and injecting current steps before and after 100 nM α -DTX application alone followed by further application of 10 μ M CCh (Fig. 10 A), similar to Fig. 8. We found that α -DTX application alone did not significantly change R_M , but subsequent

addition of CCh led to a significant increase (Fig. 10 B). AP threshold, however, decreased following application of α -DTX and even further by subsequent CCh (Fig. 10 C). AP width was unaffected by α -DTX alone or combined with CCh (Fig. 10 D). Application of α -DTX had no effect on the AHP of the initial AP, and further application of CCh led to a significant decrease (Fig. 10 E). As a consequence of lowered threshold, AP firing occurred earlier during current step injection in the presence of α -DTX, leading to a reduced AP latency that prevented any further effect by the subsequent addition of CCh (Fig. 10 F). In addition, the number of APs per step was significantly increased by α -DTX, but subsequent addition of CCh resulted in a further increase, indicating the contribution of other channels in regulating the AP firing (Fig. 10 G). Further evidence of this was shown by the instantaneous AP firing frequency. Block of D-type channels by α -DTX resulted in a significant increase, but further application of CCh caused an even greater increase in firing frequency (Fig. 10 H). AP amplitude, however, was not altered by α -DTX alone or combined with CCh (Fig. 10 I). These data show a role for D-type potassium currents in regulating the firing pattern of CA2 PNs when V_M reaches depolarized levels nearing threshold.

We also further explored the contribution of voltage-activated potassium channels by applying 100 μ M 4-AP. This compound at this concentration will effectively block all D-type potassium currents as well as potentially a fraction of A-type potassium currents. Hippocampal area CA2 has an unusually dense extracellular matrix, and we recorded very deeply within the slice to have data from healthy neurons. Both of these factors

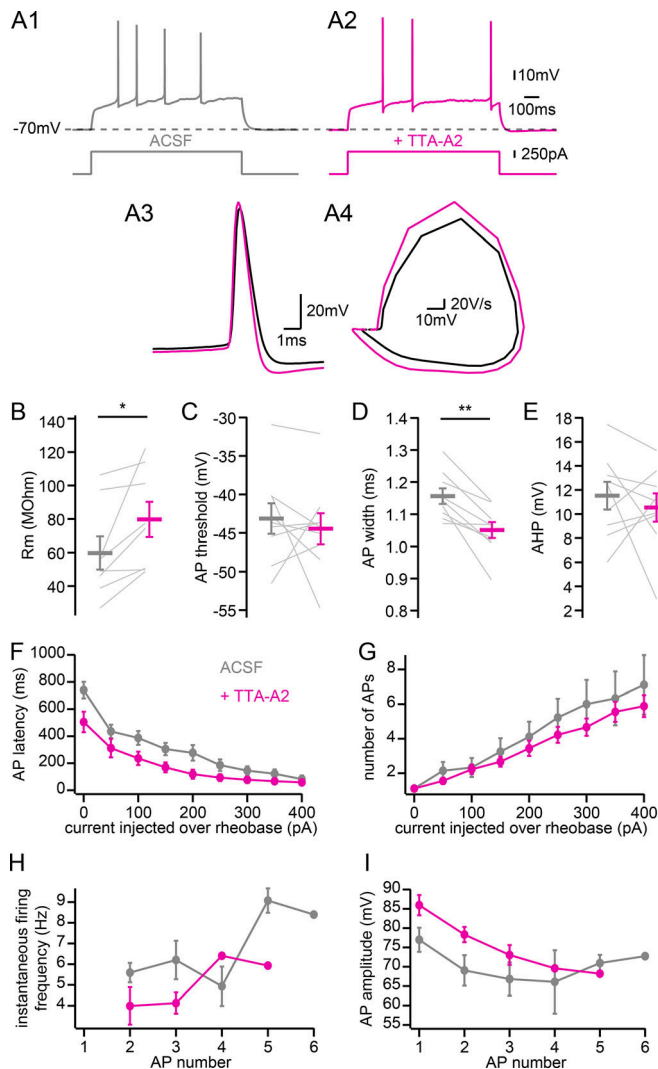


Figure 12. Influence of T-type calcium channels on CA2 PN AP firing. (A) Sample traces of AP firing in response to depolarizing current step injections recorded in whole-cell current-clamp configuration from a CA2 PN in control (A1, gray) and 2 μ M TTA-A2 (A2, magenta); expanded view of the first AP in each condition (A3); and corresponding phase plane plot (A4). (B–I) Summary graphs of CA2 PNs AP firing properties in control (gray) and 2 μ M TTA-A2 (magenta; $n = 9$; individual cells shown as thin lines; population averages shown as thick lines; error bars represent SEM). (B) R_m (before TTA-A2, 59.7 ± 9.8 MOhm; after TTA-A2, 79.8 ± 10.5 MOhm; paired t test, $P = 0.028$). (C) AP threshold (before TTA-A2, -43.1 ± 2.0 mV; after TTA-A2, -44.4 ± 2.0 mV; paired t test, $P = 0.57$). (D) AP width at half-maximal amplitude (before TTA-A2, 1.16 ± 0.02 ms; after TTA-A2, 1.05 ± 0.02 ms; paired t test, $P = 0.001$). (E) AHP (before TTA-A2, 11.5 ± 1.2 mV; after TTA-A2, 10.5 ± 1.2 mV; paired t test, $P = 0.54$). (F) Latency to fire first AP per current step as a function of current injection over rheobase (200 pA over rheobase: before TTA-A2, 276.8 ± 57.4 ms; after TTA-A2, 119.2 ± 33.8 ms; paired t test, $P = 0.077$). (G) Number of APs fired per current step as a function of current injection over rheobase (200 pA over rheobase, before TTA-A2, 4.1 ± 0.9 ; after TTA-A2, 3.4 ± 0.4 ; paired t test, $P = 0.37$). (H) Instantaneous firing frequency of APs as a function of AP number during a current step of intensity chosen 1.5 times above rheobase (first couple of APs, before TTA-A2, 5.6 ± 0.5 Hz; after TTA-A2, 4.0 ± 0.9 Hz; paired t test, $P = 0.046$). (I) AP amplitude as a function of AP number during a current step of intensity chosen 1.5 times above rheobase (first AP, before TTA-A2, 77.0 ± 3.1 mV; after TTA-A2, 85.9 ± 2.9 mV; Wilcoxon signed-rank test, $P = 0.012$). *, $P < 0.05$; **, $P < 0.01$.

make this region very challenging for pharmacology with large peptides. Unlike α -DTX, 4-AP is a small molecule that washes into the slice very quickly, allowing us to confirm the effect of α -DTX as well as examining any potential contribution from A-type currents in CA2 PN intrinsic properties before and after CCh application. When we performed the same experiment with 100 μ M 4-AP, we observed that AP firing occurred rapidly following current injection and occurred in bursts (Fig. 10 J). Apart from this major difference in initial firing pattern, we found generally similar results with 4-AP as with α -DTX for R_m (Fig. 10 K), AP threshold (Fig. 10 L), AP width (Fig. 10 M), and number of APs per step (Fig. 10 P). Furthermore, we observed effects from 4-AP application that were likely not due to D-type potassium channel block. Strikingly, the AHP was abolished (Fig. 10 N), which likely led to the high-frequency AP bursting early in the current step. We also observed a very short AP latency (Fig. 10 O) and very high initial firing rate (Fig. 10 Q). Consistent with the AP threshold markedly lowered by 4-AP and 4-AP plus CCh, the amplitude of the first AP was higher in these conditions (Fig. 10 R). We conclude from this dataset that 100 μ M 4-AP likely acts on D-type and other potassium currents that contribute to the firing pattern of CA2 PNs.

Next, we assessed the contribution of voltage-activated potassium current to spontaneous burst firing by recording CA2 PNs in passive current-clamp mode and applying 100 nM α -DTX or 100 μ M 4-AP followed by 10 μ M CCh (Fig. 11 A). Consistent with D-type potassium channels being opened at only depolarized V_M levels (Storm, 1988), application of α -DTX or 4-AP did not change the resting V_M , while subsequent application of CCh caused an initial depolarization similar to control conditions (Fig. 11, B1 and B2). The main effect of blocking D-type potassium currents was an accelerated rise of V_M at the onset of bursts seen with both α -DTX and 4-AP (Fig. 11 C and Table 2). Other effects with 4-AP potentially not restricted to D-type potassium currents were a faster burst decay rate (Fig. 4 D and Table 2) and increased firing rate during bursts (Fig. 4 E and Table 2). Other burst parameters were unchanged by α -DTX or 4-AP (Table 2). Altogether, these experiments show a key role of D-type potassium currents in controlling the early phase of burst firing induced by CCh in CA2 PNs.

T-type calcium currents control the duration of CA2 PN AP bursts

T-type calcium channels are activated at V_M values near rest and cause transient calcium influx that depolarizes neurons. These channels are involved in setting the resting V_M in cortical neurons (Hu and Bean, 2018) and can be activated by cholinergic stimulation in the dentate gyrus granule cells (Martinello et al., 2015). We hypothesize that these channels may be expressed in CA2 PNs and may play a role in regulating the rhythmic bursting activity of these cells. These channels are expressed widely in the hippocampus, including area CA2 (Tang et al., 2011). To determine how T-type calcium channels contribute to the intrinsic properties of CA2 PNs, we performed whole-cell current clamp experiments and injected current steps before and after blocking T-type channels with 2 μ M TTA-A2 (Fig. 12 A). We found that TTA-A2 caused an increase in R_m (Fig. 12 B). Blocking

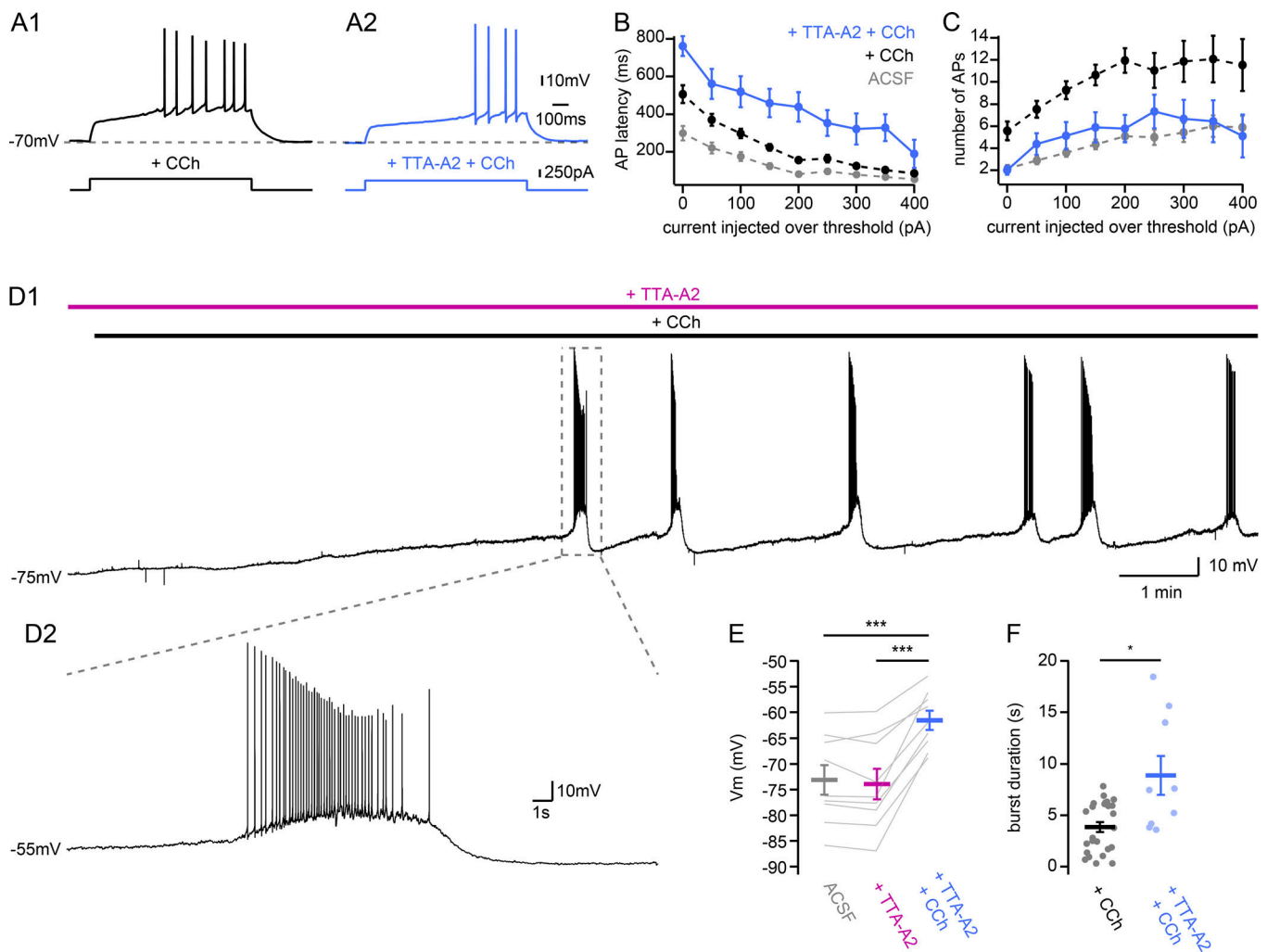


Figure 13. **T-type voltage-gated calcium channels control the duration of CCh-induced bursts in CA2 PNs.** (A) Sample traces of AP firing in response to depolarizing current step injections recorded in whole-cell current-clamp configuration from CA2 PNs in 10 μM CCh (A1, black) or 2 μM TTA-A2 and 10 μM CCh (A2, blue). (B and C) Summary graphs of CA2 PN intrinsic properties in 10 μM CCh (CCh, black; ACSF gray; n = 34; for reference, same CCh and control data as shown in Fig. 3, F and G), and 2 μM TTA-A2 and 10 μM CCh (blue, n = 9; population averages shown as thick lines; error bars represent SEM). (B) Latency to fire first AP per current step by CA2 PNs as a function of current injection over rheobase (200 pA over rheobase, CCh, 156.0 ± 15.0 ms; CCh and TTA-A2, 438.4 ± 77.7 ms; Mann-Whitney U test, P < 0.001). (C) Number of APs fired per current step by CA2 PNs as a function of current injection over rheobase (200 pA over rheobase, CCh, 11.9 ± 1.1; CCh and TTA-A2, 5.8 ± 1.2; t test, P = 0.001). (D) Sample trace of bursts recorded in whole-cell current-clamp configuration from a CA2 PN (D1) and expanded view of a burst (D2) upon application of 10 μM CCh in acute hippocampal slice with T-type voltage-gated calcium channels blocked by application of 2 μM TTA-A2. (E) V_M levels at rest (gray), after application of 2 μM TTA-A2 (magenta), and after further application of 10 μM CCh (blue; before TTA-A2, -73.1 ± 2.9 mV; after TTA-A2, -73.9 ± 3.0 mV; after TTA-A2 and CCh V_M, -61.7 ± 1.8 mV, n = 9; repeated-measures ANOVA, P < 0.001). (F) Summary graph of CA2 PN AP burst duration with application of 10 μM CCh in control (black, n = 25; same CCh data shown in Fig. 14 F as 10 μM CCh in Fig. 1 E) and 2 μM TTA-A2 (blue, n = 9; Mann-Whitney U test, P = 0.006; individual cells shown as dots; population averages shown as thick lines; error bars represent SEM). *, P < 0.05; ***, P < 0.001.

these channels had no effect on AP threshold (Fig. 12 C) but did result in a decrease in the AP width (Fig. 12 D), whereas there was no change in AHP (Fig. 12 E). Furthermore, we observed no change in AP latency or number of APs (Fig. 12, F and G). After blocking T-type channels, we did observe a small but significant change in firing frequency and an increase in AP amplitude (Fig. 12, H and I). From these experiments, we can conclude that T-type calcium channels are expressed by CA2 PNs and contribute to several aspects of their intrinsic AP firing properties, including the timing of AP firing when the cell becomes depolarized.

Given these observations, we hypothesize that blocking T-type calcium channels may potentially alter the properties of CCh-induced rhythmic AP bursting. To test this, we first performed current clamp experiments in which we held the cells at -70 mV and progressively injected depolarizing steps of current in the presence of CCh alone or with application of CCh plus 2 μM TTA-A2 (Fig. 13 A). Blocking T-type channels significantly increased AP latency (Fig. 13 B) and effectively prevented the CCh-induced increase in AP firing (Fig. 13 C). Therefore, T-type calcium channels are likely involved in the modification of AP firing induced by CCh in CA2 PNs, opening with

Table 3. Effect of TTA-A2 on charbachol-induced CA2 PN spontaneous activity

Measurement	Control (<i>n</i> = 25)	T-type voltage-gated calcium channels blocked (2 μ M TTA-A2; <i>n</i> = 9)	Statistics
ACSF- V_M (mV)	-75 ± 1.2	-72 ± 2.3	$P = 0.28^a$
CCh- V_M (mV)	-64 ± 1.0	-62 ± 1.8	$P = 0.22^a$
$\Delta_{\text{ACSF-CCh}} V_M$ (mV)	11 ± 1.0	11 ± 1.0	$P = 0.89^b$
Depolarization rate (mV/min)	6.5 ± 0.8	4.6 ± 0.9	$P = 0.12^a$
Burst onset (min)	6.4 ± 0.7	6.0 ± 1.0	$P = 0.78^a$
Interburst interval (s)	100 ± 14.7	109 ± 18.4	$P = 0.74^a$
Burst- V_M (mV)	-42 ± 1.0	-42 ± 0.7	$P = 0.74^b$
Interburst- V_M (mV)	-62 ± 0.8	-60 ± 1.2	$P = 0.17^a$
$\Delta_{\text{burst-IBI}} V_M$ (mV)	21 ± 1.2	18 ± 0.9	$P = 0.13^b$
Burst rise rate (mV/s)	3.5 ± 0.5	2.8 ± 0.5	$P = 0.69^b$
Burst decay rate (mV/s)	-4.6 ± 0.8	-5.1 ± 1.1	$P = 0.83^b$
Burst duration (s)	3.8 ± 0.5	8.9 ± 1.9	$P = 0.006^b$
Number of APs/burst	22 ± 2.5	31 ± 6.4	$P = 0.072^b$
Firing frequency in burst (Hz)	13 ± 1.9	10 ± 1.9	$P = 0.66^b$

^at test.

^bMann-Whitney *U* test.

membrane depolarization and contributing to further depolarization and AP firing. Blocking these channels reveals this contribution. The decrease in the number of APs during the 1 s current injection step in the presence of CCh could potentially be due to the increased AP latency.

We next examined the effects of TTA-A2 on CCh-induced spontaneous AP bursts in CA2 PNs (Fig. 13 D). TTA-A2 block of T-type channels did not significantly change the resting V_M level of CA2 PNs and did not affect their initial depolarization by CCh (Fig. 13 E). However, we found that application of TTA-A2 before CCh application resulted in a significant increase in the duration of AP bursts (Fig. 13 F and Table 3), while all other burst properties were unchanged (Table 3). Therefore, we conclude that T-type calcium channels are involved in controlling the duration of bursts, potentially by regulating calcium influx before and during AP burst firing that would eventually contribute to ending the burst by activating calcium-dependent potassium channels.

Small-conductance calcium-activated K⁺ channels contribute to CA2 PN V_M repolarization between bursts

Sustained AP firing and V_M depolarization as seen in CA2 PNs during CCh-induced AP bursting can lead to calcium influx and activation of calcium-activated potassium channels. In several types of neurons, SK channels frequently underlie a major component of the afterhyperpolarizing current following single or bursts of APs, acting to regulate burst firing (Stocker, 2004). In CA1 hippocampal pyramidal cells, these channels have been shown to be less important than K_V7 channels in regulating excitability (Chen et al., 2014). However, it has been shown that transient activation of M1 mAChRs does activate the store-release inositol triphosphate-mediated pathway that acts via SK

channels to transiently control membrane excitability (Dasari et al., 2017). To examine this further, we first sought to establish the presence of SK channels in CA2 PNs and their contribution to AP firing by injecting current steps before and after application of 0.1 μ M apamin (Fig. 14 A). While we found no change in R_M (Fig. 14 B), we did measure a small but significant decrease in AP threshold (Fig. 14 C), as well as a decrease in AP width (Fig. 14 D) and an increase in AHP amplitude (Fig. 14 E). This change in AHP is puzzling to us and merits further study. Blocking SK channels had fairly minor or no effect on other aspects of CA2 PN firing (Fig. 14, F-I).

While apamin had minimal effects on CA2 PN AP firing, they are consistent with an increased R_M that would be expected when blocking a potassium channel, thus warranting the study of SK channel contributions to the effects of CCh on CA2 PNs. To examine this further, we recorded pyramidal cells in area CA2 and injected depolarizing current steps in the presence of 10 μ M CCh with and without 0.1 μ M of apamin (Fig. 15 A). Block of SK channels by apamine resulted in increased AP latency in the presence of CCh (Fig. 15 B). Furthermore, blocking these channels appeared to prevent the CCh-induced increase in AP number with each current injection step (Fig. 15 C). The increased latency that we observed following CCh application when SK channels were blocked merits further study. Perhaps the block of SK allows increased influx of calcium that permits the activation of large-conductance calcium-activated potassium channels (BK channels), further hyperpolarizing the cells and delaying AP firing.

To determine how SK channels potentially contribute to CCh-induced spontaneous bursting of CA2 PNs, we recorded these cells in the presence of apamin followed by CCh application (Fig. 15 D). Block of SK channels by apamin alone did not

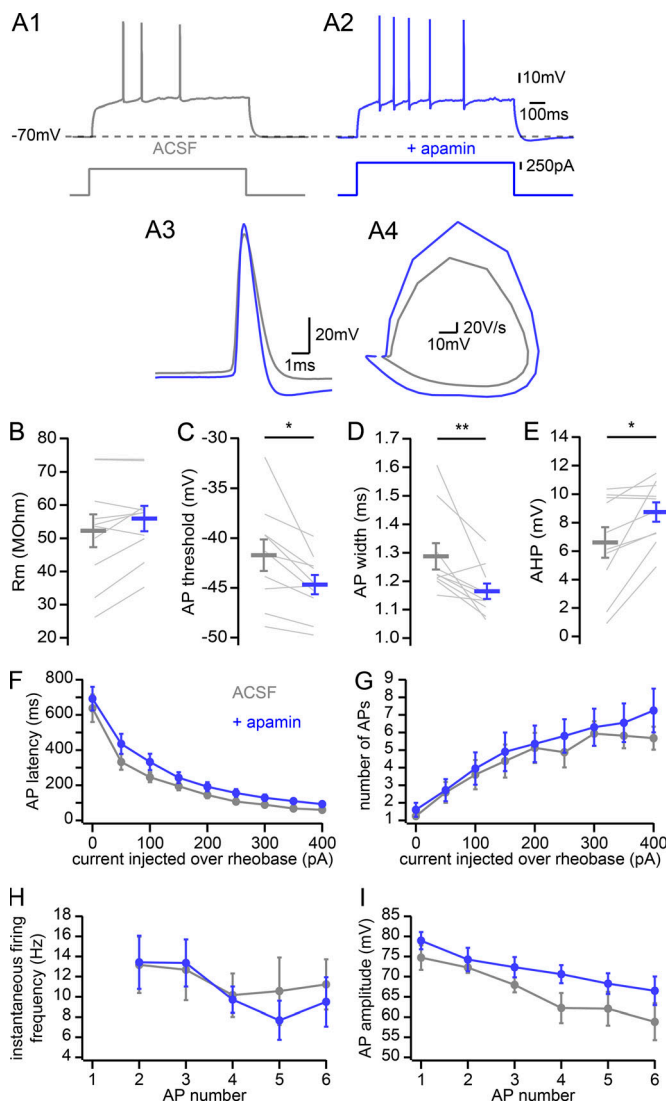


Figure 14. Influence of SK channels on CA2 PN AP firing. (A) Sample traces of AP firing in response to depolarizing current step injections recorded in whole-cell current-clamp configuration from a CA2 PN in control (A1, gray) and 0.1 μM apamin (A2, blue); expanded view of the first AP in each condition (A3) and corresponding phase plane plot (A4). (B–I) Summary graphs of CA2 PNs AP firing properties in control (gray) and 0.1 μM apamin (blue; $n = 10$; individual cells shown as thin lines; population averages shown as thick lines; error bars represent SEM). (B) R_M (before apamin, 52.2 ± 5.0 MΩ; after apamin, 55.9 ± 3.8 MΩ; paired t test, $P = 0.053$). (C) AP threshold (before apamin, -41.7 ± 1.6 mV; after apamin, -44.7 ± 1.0 mV; paired t test, $P = 0.010$). (D) AP width at half-maximal amplitude (before apamin, 1.29 ± 0.05 ms; after apamin, 1.16 ± 0.03 ms; Wilcoxon signed-rank test, $P = 0.006$). (E) AHP (before apamin, 6.6 ± 1.1 mV; after apamin, 8.7 ± 0.7 mV; paired t test, $P = 0.013$). (F) Latency to fire first AP per current step as a function of current injection over rheobase (200 pA over rheobase, before apamin, 144.9 ± 18.5 ms; after apamin, 191.3 ± 25.6 ms; paired t test, $P = 0.087$). (G) Number of APs fired per current step as a function of current injection over rheobase (200 pA over rheobase, before apamin, 5.1 ± 0.9 ; after apamin, 5.4 ± 1.0 ; paired t test, $P = 0.60$). (H) Instantaneous firing frequency of APs as a function of AP number during a current step of intensity chosen 1.5 times above rheobase (first couple of APs, before apamin, 13.2 ± 2.8 Hz; after apamin, 13.4 ± 2.6 Hz; paired t test, $P = 0.74$). (I) AP amplitude as a function of AP number during a current step of intensity chosen 1.5 times above rheobase (first AP, before apamin, 74.7 ± 3.0 mV; after apamin, 79.0 ± 2.1 mV; Wilcoxon signed-rank test on first AP amplitude, $P = 0.13$). *, $P < 0.05$; **, $P < 0.01$.

depolarize CA2 PNs, and subsequent application of CCh resulted in a significant depolarization (Fig. 15 E) very similar to what we observed with CCh application alone (Table 4). Nearly all properties of the AP bursts were unchanged by the presence of apamin (Table 4). However, we did observe an increase in the V_M between bursts, indicating that blocking SK channels disrupts the repolarization of the membrane (Fig. 15 F). Thus, our observations are very similar to reports for CA1 PNs (Chen et al., 2014), showing that SK channels contribute in a relatively minor way to regulating spontaneous AP bursting under conditions following mACh activation.

Discussion

Using patch-clamp recordings in acute hippocampal slices from adult mice, we report several changes in hippocampal CA2 PN properties following mAChR activation. In summary, application of 10 μM CCh led to a depolarization of the V_M and rhythmic bursts of AP firing. We found that the membrane depolarization would occur with 1 μM CCh, whereas the burst firing required higher concentrations. 10 μM CCh altered several intrinsic properties of CA2 PNs, including the R_M , AP threshold, AP width, AHP, latency, AP number, AP firing frequency, and sag current. While several aspects of the spontaneous AP bursting kinetics are shaped by excitatory and inhibitory synaptic transmission, CA2 PNs were found to be capable of spontaneously firing bursts of APs with all transmission blocked. Upon examination of synaptic transmission, we observed that CCh application attenuated both excitatory and inhibitory transmission. Lastly, we examined the contributions of the potassium M-current from K_{V7} ion channels, T-type calcium channels, D-type potassium channels, and SK channels to the intrinsic properties and AP bursting of CA2 PNs, finding that they play roles in regulating the excitability and AP firing of these cells.

The influence of the muscarinic tone on hippocampal physiology has long been recognized and extensively studied in area CA3 and CA1. Application of cholinergic agonists or stimulation of cholinergic inputs in acute hippocampal slices has been found to result in the depolarization of resting V_M and an increase in R_M in CA3 and CA1 PNs (Dodd et al., 1981; Cole and Nicoll, 1983, 1984). In area CA2, we found that low concentrations of CCh resulted in V_M depolarization. We also found that blocking the M1 and M3 muscarinic receptors effectively prevented depolarization and all spontaneous bursting activity. This is consistent with what has previously been described in CA3 PNs (Williams and Kauer, 1997). Furthermore, these findings are consistent with immunohistological evidence that M1 and M3 receptors are expressed in area CA2 (Levey et al., 1995). The pharmacological methods that we used in this paper support the premise that M1/M3 muscarinic acetylcholine receptors are expressed in CA2 PNs, as application of 1 μM 4-DAMP and 10 μM Pirenzepine prevents the large depolarization of the resting V_M by CCh application and completely prevents spontaneous AP bursting. At 1 μM, a small fraction of M1 mAChRs would be expected to be blocked by 4-DAMP (Caulfield and Birdsall, 1998), and concrete discrimination between these two subtypes with our dataset cannot be done. Closer examination of RNA levels for different muscarinic receptor subtypes available on

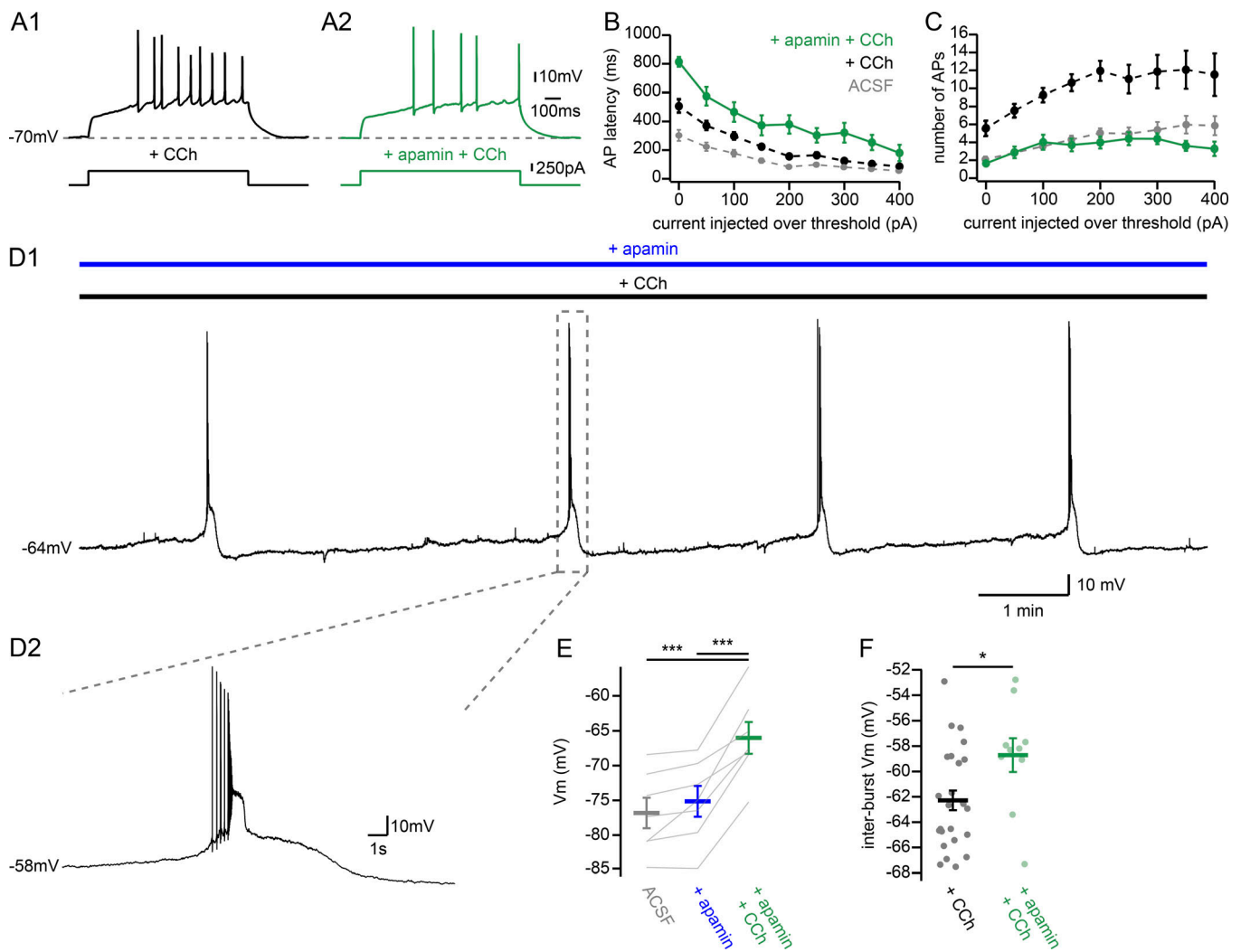


Figure 15. SK channels contribute to CA2 PN V_m repolarization at the end of AP bursts. (A) Sample traces of AP firing in response to depolarizing current step injections recorded in whole-cell current-clamp configuration from CA2 PNs in 10 μM CCh (A1, black) or 0.1 μM apamin and 10 μM CCh (A2, green). (B and C) Summary graphs of CA2 PN intrinsic properties in 10 μM CCh (CCh, black; ACSF, gray; $n = 34$; for reference, same CCh and control data as shown in Fig. 3, F and G), and 0.1 μM apamin and 10 μM CCh (green, $n = 10$; population averages shown as thick lines; error bars represent SEM). (B) Latency to fire first AP per current step by CA2 PNs as a function of current injection over rheobase (200 pA over rheobase, CCh, 156 ± 15.0 ms; CCh and apamin, 379 ± 64 ms; Mann-Whitney U test, $P < 0.001$). (C) Number of APs fired per current step by CA2 PNs as a function of current injection over rheobase (200 pA over rheobase, CCh, 11.9 ± 1.1 ; CCh and apamin, 4.0 ± 0.7 ; Mann-Whitney U test, $P < 0.001$). (D) Sample trace of bursts recorded in whole-cell current-clamp configuration from a CA2 PN (D1) and expanded view of a burst (D2) upon application of 10 μM CCh in acute hippocampal slice with SK channels blocked by application of 0.1 μM apamin. (E) V_m levels at resting (gray), after application of 0.1 μM apamin (blue), and after further application of 10 μM CCh (green; before apamin V_m , -76.8 ± 2.2 mV; after apamin V_m , -75.1 ± 2.2 mV; after apamin and CCh V_m , -66.0 ± 2.3 mV, $n = 7$; repeated-measures ANOVA, $P < 0.001$). (F) Summary graph of CA2 PN V_m level in between bursts with application of 10 μM CCh in control (black, $n = 25$; same CCh data shown in Fig. 14 F as CCh in Fig. 4 G) and 0.1 μM apamin (green, $n = 10$; t test, $P = 0.035$; individual cells shown as dots; population averages shown as thick lines; error bars represent SEM). *, $P < 0.05$; ***, $P < 0.001$.

the Allen Brain Atlas (<http://mouse.brain-map.org/gene/show/12456>) show that the relative levels of the M3 mAChR are lower in area CA2 compared with areas CA1 and CA3. This difference is intriguing, as different effects on PN depolarization and plasticity have previously been attributed to M3 and M1 mAChRs (Pitler and Alger, 1990; Auerbach and Segal, 1996). Furthermore, our results indicate that potential differences in downstream Gq/11 downstream signaling cascades in area CA2 merit further investigation. There is already evidence from studies examining RGS14, and its role in preventing NMDA-mediated long-term plasticity, indicating that intracellular signaling pathways diverge in area CA2 compared with CA1 and CA3 (Lee et al., 2010; Evans et al., 2018).

These results demonstrate that CA2 PNs express muscarinic acetylcholine receptors that inhibit the M-current upon activation by CCh. We found that pharmacologically blocking the M-current led to a statistically significant depolarization of the V_m , albeit only a fraction of the depolarization observed with CCh. The extent of the depolarization that we observed following application of XE-991 is slightly lower than what had been reported in another study (3.2 ± 0.6 compared with 4.2 ± 0.5 mV; Tirko et al., 2018). In our experiments, we used a K-methanesulfonate-based solution while Tirko et al. (2018) used a K-gluconate-based intracellular solution. We hypothesize that this difference in intracellular solution may underlie the differences in cellular excitability that we observed

Table 4. Effect of apamin on charbachol-induced CA2 PN spontaneous activity

Measurement	Control (<i>n</i> = 25)	SK channels blocked (0.1 μM apamin; <i>n</i> = 10)	Statistics
ACSF- V_M (mV)	-75 ± 1.2	-75 ± 2.2	$P = 0.95^a$
CCh- V_M (mV)	-64 ± 1.0	-66 ± 2.3	$P = 0.49^a$
$\Delta_{\text{ACSF-CCh}} V_M$ (mV)	11 ± 1.0	9.1 ± 1.3	$P = 0.55^b$
Depolarization rate (mV/min)	6.5 ± 0.8	5.3 ± 1.6	$P = 0.50^a$
Burst onset (min)	6.4 ± 0.7	6.5 ± 1.3	$P = 0.93^a$
Interburst interval (s)	100 ± 14.7	120 ± 31.2	$P = 0.58^a$
Burst- V_M (mV)	-42 ± 1.0	-42 ± 1.2	$P = 0.41^a$
Interburst- V_M (mV)	-62 ± 0.8	-59 ± 1.3	$P = 0.035^a$
$\Delta_{\text{burst-IBI}} V_M$ (mV)	21 ± 1.2	17 ± 1.9	$P = 0.045^a$
Burst rise rate (mV/s)	3.5 ± 0.5	5.6 ± 1.2	$P = 0.06^b$
Burst decay rate (mV/s)	-4.6 ± 0.8	-4.7 ± 1.0	$P = 0.91^b$
Burst duration (s)	3.8 ± 0.5	5.4 ± 1.9	$P = 0.97^b$
Number of APs/burst	22 ± 2.5	16 ± 2.0	$P = 0.20^b$
Firing frequency in burst (Hz)	13 ± 1.9	12 ± 3.0	$P = 0.94^b$

^at test.

^bMann–Whitney *U* test.

following XE-991 application. Intracellular gluconate has been shown to inhibit several currents, including I_K , I_{AHP} , I_h , and I_{Ca} currents, resulting in higher R_M and altered AP firing properties (Velumian et al., 1997). Furthermore, intracellular gluconate has been shown to alter the calcium dynamics of the calyx of Held, indicating that this counterion potentially buffers intracellular calcium (Woehler et al., 2014). Consistent with this, we measured R_M values in CA2 PNs appreciably lower than those reported in Tirko et al. (2018), and the resting V_M was also more hyperpolarized. Thus, with the difference in R_M and lower starting value, our blocking of the M-current with XE-991 did not sufficiently depolarize the membrane to allow spontaneous AP bursting.

Subsequent application of CCh led to further V_M depolarization of ~6 mV, indicating the contribution of an additional current following muscarinic activation. That we had a valid positive control for XE-991 application, and that several actions of CCh were occluded by XE-991 application, suggests that the drug was fairly efficient at blocking K_V7 . It has been reported that activation of M1 mAChRs can activate a nonselective cation conductance (Shalinsky et al., 2002; Haj-Dahmane and Andrade, 1996) that could readily result in membrane depolarization. Furthermore, a clear link has been made between M1 mAChR activation and inositol triphosphate-mediated signaling (Dasari et al., 2017; Dasari and Gullledge, 2011). We postulate here that these mechanisms may also be at play in CA2 PNs. One major weakness of our work in this study is prolonged application of CCh to activate all mAChRs. While this does allow for the fundamental molecular players to be identified, ACh is released in a pulsatile manner in vivo, and there is likely more complex signaling occurring at short time dynamics that merit future investigation. Differences have been reported between the phasic cholinergic signaling in areas CA1 and CA3 (Gullledge

and Kawaguchi, 2007), and it would be interesting to know how CA2 responds under these conditions. From our results here, we would predict that CA2 PNs would look more like CA1 than CA3, but further investigation is needed. With the use of ACh, a second future question worth investigating is the potential role of nAChRs in synaptic plasticity in area CA2. It has previously been shown that activation of $\alpha 7$ nAChRs leads to postsynaptic plasticity in hippocampal CA1 PN neurons (Halff et al., 2014). As the calcium dynamics in area CA2 have been shown to prevent NMDA-mediated long-term potentiation (Simons et al., 2009), determining if and how nAChR activation participates in synaptic plasticity in this area is an interesting avenue of research.

In addition to the M-current, we also explored a potential role of D-type potassium current in regulating CA2 cellular excitability and spontaneous AP bursting in high muscarinic tone. Activation of M1 muscarinic receptors results in depletions of PIP_2 (Hackelberg and Oliver, 2018). This PIP_2 depletion can potentially result in the modification of gating of several voltage-gated potassium currents (Rodríguez-Menchaca et al., 2012). It is possible that several of the effects of CCh on the AP firing and bursting may be due to an increase in D-type current. This quickly activating but slowly inactivating current has been shown to be very important for regulating AP timing and network synchrony in areas CA1 and CA3 (Storm, 1988; Cudmore et al., 2010). Our results indicate that in area CA2, this current indeed plays a considerable role in regulating spike precision as well as several aspects of CCh-induced AP bursting.

For CA3 and CA1 PNs, several different effects of CCh application on AP firing have been reported. These include spontaneous burst firing (Cobb et al., 1999), transformation of current injection-evoked single spikes into bursts (Yue et al., 2005), and

induction of persistent firing after current injection-evoked depolarization (Jochems and Yoshida, 2013; Knauer et al., 2013). Our experiments in CA2 PNs demonstrate that CCh application causes CA2 PNs to fire bursts of APs in a way that is very similar to CA3 PNs under similar conditions (Cobb et al., 1999). In this study, we demonstrated the role of T-type calcium channels in controlling the duration of these AP bursts in CA2 PNs. This finding is consistent with other cell types, as calcium currents have been known to be important for CA3 PN AP bursting (MacVicar and Tse, 1989). Furthermore, T-type calcium channels are partially opened near resting V_M levels in cortical neurons (Hu and Bean, 2018), and their activation by muscarinic stimulation causes calcium entry in dentate gyrus granule cells (Martinello et al., 2015). In dopaminergic midbrain neurons, intrinsic bursting is regulated by coupled activity of T-type and SK channels (Wolfart and Roeper, 2002). In CA2 PNs, we show that SK channels are involved in the repolarization of V_M following bursts. Thus, it may be possible that a similar mechanism is at play in these cells: that prolonged AP firing during bursts allows calcium influx that activates calcium-activated potassium channels, terminating the burst. Further work is required to better understand the calcium channel composition and contribution to excitability in CA2 pyramidal cells.

We did not investigate the potential role of large-conductance calcium-activated potassium channels in regulating the CCh-induced burst firing in this study. BK channels have been shown to be important for enabling high-frequency AP firing and early spike frequency adaptation in CA1 PNs (Gu et al., 2007), two properties that are nearly absent in CA2 PNs. That does not mean, however, that these channels are not contributing in a central way to the active properties of CA2 PN dendrites. In fact, given the unusual calcium buffering of CA2 PNs (Simons et al., 2009; Evans et al., 2018) and its implications for synaptic plasticity, the role of BK channels, and their possible interaction with SK channels in regulating AP firing in CA2, merits further investigation.

Of note, we saw that synaptic transmission played a role in shaping AP bursting frequency, duration, and V_M between bursts. In our acute slice preparations, excitatory inputs to area CA2 originated from CA3 PNs, from recurrent connections from CA2 PNs, and from the entorhinal cortex. When these inputs are blocked, CA2 PNs fire fewer APs per burst and repolarize less after bursts. Excitatory transmission is likely important to sustain AP firing during bursts, which potentially contributes to allow calcium influx in CA2 PNs as well as promote subsequent repolarization of the V_M to start a new burst. Removal of inhibitory transmission transformed bursts of APs into sudden brief AP discharges in which APs fired at higher frequency and rapidly hyperpolarized. Blocking excitatory transmission alone appeared to be indistinguishable from blocking all synaptic transmission. Clearly, feed-forward and feedback inhibition plays a central role in regulating overall excitability and AP firing in area CA2.

Interestingly, AP burst firing by CA2 PNs has recently been described to be induced by oxytocin (Tirko et al., 2018). These bursts of APs were mediated by PLC-mediated reduction of the M-current and activation of PKC. The oxytocin receptor-mediated AP bursts described by Tirko et al. (2018) lasted on the order of 2–3 s and had a firing frequency of ~14 Hz, similar to the CCh-induced bursts that we report here. A question for future research will be to determine

the downstream intracellular signaling pathways activated by M1 and M3 muscarinic receptors in CA2 PNs and how they are similar to those of other receptors. This question is very pertinent for CA2 PNs, as numerous G protein and growth factor receptors are either enriched or exclusively expressed in this region. These include the adenosine A1 receptor (Ochiishi et al., 1999), vasopressin 1b receptor (Young et al., 2006), and epidermal growth factor receptor (Tucker et al., 1993). Thus, having a better understanding of how the activity of CA2 PNs is altered in the presence and absence of high muscarinic tone is an important first step in fully understanding how this hippocampal area is affected by these signaling molecules.

The hippocampus receives a major cholinergic input from the septum (Amaral and Kurz, 1985); therefore, the hippocampal cholinergic tone is likely high when septal cholinergic neurons are active, during active exploration. It is well accepted that area CA2 plays a critical role in social memory formation (Hitti and Siegelbaum, 2014; Stevenson and Caldwell, 2014), and we predict that during social exploratory behaviors, cholinergic tone is likely to be elevated, influencing the cellular properties of CA2 PNs in a way similar to what we characterize in this paper. Major questions remain concerning how social information is encoded by the hippocampus and the precise role of area CA2 in this process. During social exploration, CA2 PNs likely receive theta-locked inputs from the entorhinal cortex, the septum, the supramammillary nucleus, and area CA3 (Robert et al., 2018). Our results indicate that changes in the V_M resulting from M1 and M3 activation in high cholinergic tone suppress CA3 inputs more than cortical inputs, as has been observed in other CA regions (Kremen and Hasselmo, 2007; Hasselmo and Schnell, 1994). These diverse inputs would be summated, and the resulting CA2 output will then impact area CA1, CA3, and extrahippocampal structures. Our results will be a necessary tool for modeling and in vivo studies that consider area CA2 in the hippocampus.

Lastly, understanding the function and physiological mechanisms of CA2 PNs is important in the context of psychiatric and neurological disorders, as this region has been shown to undergo changes in human postmortem studies and animal models of schizophrenia (Benes et al., 1998; Piskorowski et al., 2016) and several other neuropsychiatric and neurodegenerative diseases (Chevalyere and Piskorowski, 2016). Notably, the density of cholinergic input as well as acetylcholinesterase have been found to be decreased in patients with Alzheimer's disease, most dramatically in area CA2 compared with other hippocampal areas (Ransmayr et al., 1989). Furthermore, it has recently been proposed that cholinergic dysfunction contributes to cognitive decline in Parkinson's disease and is associated with increased Lewy pathology within the CA2 region (Liu et al., 2019).

Acknowledgments

Richard W. Aldrich served as guest editor.

Some of the experiments were performed at the Neurobiology course at the Woods Hole Marine Biology Laboratory. We thank Philippe Ascher, Jean Christophe Poncer, Karim Benchene, Audrey Mercer, Liset Mendez de la Prida, and Paul Salin for their constructive input. Some of these experiments were

performed in the laboratory of Jayeeta Basu at New York University, and we thank the Basu lab for their support.

This work was supported by the Fondation pour la Recherche Médicale (FTD20170437387 to V. Robert). R.A. Piskorowski was supported by a National Alliance for Research on Schizophrenia and Depression independent investigator grant from the Brain and Behavior Research Foundation, funding from the Ville de Paris Program Emergences, and Agence Nationale de la Recherche (ANR-13-JSV4-0002-01 project HypoHippo and ANR-18-CE37-0020-01 project WhoRU). M.F. Davatolhagh was supported by the Howard Hughes Medical Institute Gilliam Fellowship.

The authors declare no competing financial interests.

Author contributions: Conceptualization, V. Robert, V. Chevaleyre, and R.A. Piskorowski; Investigation, R.A. Piskorowski, V. Robert, and V. Chevaleyre performed electrophysiology; R.A. Piskorowski, and L. Therreau performed immunohistology; M.F. Davatolhagh, F.J. Bernardo-Garcia, and K.N. Clements contributed to the experiments on evoked synaptic transmission; Analysis, V. Robert, V. Chevaleyre, and R.A. Piskorowski; Writing, R.A. Piskorowski, V. Chevaleyre, and V. Robert; Funding acquisition, R.A. Piskorowski, and V. Robert; Resources, R.A. Piskorowski and V. Chevaleyre.

Submitted: 30 July 2019

Revised: 18 December 2019

Accepted: 13 January 2020

References

- Amaral, D.G., and J. Kurz. 1985. An analysis of the origins of the cholinergic and noncholinergic septal projections to the hippocampal formation of the rat. *J. Comp. Neurol.* 240:37–59. <https://doi.org/10.1002/cne.902400104>
- Auerbach, J.M., and M. Segal. 1996. Muscarinic receptors mediating depression and long-term potentiation in rat hippocampus. *J. Physiol.* 492: 479–493. <https://doi.org/10.1113/jphysiol.1996.sp021323>
- Benes, F.M., E.W. Kwok, S.L. Vincent, and M.S. Todtenkopf. 1998. A reduction of nonpyramidal cells in sector CA2 of schizophrenics and manic depressives. *Biol. Psychiatry.* 44:88–97. [https://doi.org/10.1016/S0006-3223\(98\)00138-3](https://doi.org/10.1016/S0006-3223(98)00138-3)
- Botcher, N.A., J.E. Falck, A.M. Thomson, and A. Mercer. 2014. Distribution of interneurons in the CA2 region of the rat hippocampus. *Front. Neuroanat.* 8:104. <https://doi.org/10.3389/fnana.2014.00104>
- Brown, D.A., and P.R. Adams. 1980. Muscarinic suppression of a novel voltage-sensitive K⁺ current in a vertebrate neurone. *Nature.* 283: 673–676. <https://doi.org/10.1038/283673a0>
- Caulfield, M.P., and N.J. Birdsall. 1998. International Union of Pharmacology. XVII. Classification of muscarinic acetylcholine receptors. *Pharmacol. Rev.* 50:279–290.
- Chen, S., F. Benninger, and Y. Yaari. 2014. Role of Small Conductance Ca²⁺-Activated K⁺ Channels in Controlling CA1 Pyramidal Cell Excitability. *J. Neurosci.* 14:8219–8230.
- Chevaleyre, V., and R.A. Piskorowski. 2016. Hippocampal Area CA2: An Overlooked but Promising Therapeutic Target. *Trends Mol. Med.* 22: 645–655. <https://doi.org/10.1016/j.molmed.2016.06.007>
- Cobb, S.R., and C.H. Davies. 2005. Cholinergic modulation of hippocampal cells and circuits. *J. Physiol.* 562:81–88. <https://doi.org/10.1113/jphysiol.2004.076539>
- Cobb, S.R., D.O. Bulters, S. Suchak, G. Riedel, R.G. Morris, and C.H. Davies. 1999. Activation of nicotinic acetylcholine receptors patterns network activity in the rodent hippocampus. *J. Physiol.* 518:131–140. <https://doi.org/10.1111/j.1469-7793.1999.0131r.x>
- Cole, A.E., and R.A. Nicoll. 1983. Acetylcholine mediates a slow synaptic potential in hippocampal pyramidal cells. *Science.* 221:1299–1301. <https://doi.org/10.1126/science.6612345>
- Cole, A.E., and R.A. Nicoll. 1984. Characterization of a slow cholinergic postsynaptic potential recorded in vitro from rat hippocampal pyramidal cells. *J. Physiol.* 352:173–188. <https://doi.org/10.1113/jphysiol.1984.sp015285>
- Cudmore, R.H., L. Fronzaroli-Molinieres, P. Giraud, and D. Debanne. 2010. Spike-time precision and network synchrony are controlled by the homeostatic regulation of the D-type potassium current. *J. Neurosci.* 30: 12885–12895. <https://doi.org/10.1523/JNEUROSCI.0740-10.2010>
- Dasari, S., and A.T. Gullledge. 2011. M1 and M4 receptors modulate hippocampal pyramidal neurons. *J. Neurophysiol.* 105:779–792. <https://doi.org/10.1152/jn.00686.2010>
- Dasari, S., C. Hill, and A.T. Gullledge. 2017. A unifying hypothesis for M1 muscarinic receptor signalling in pyramidal neurons. *J. Physiol.* 595: 1711–1723. <https://doi.org/10.1113/JP273627>
- de N6, R.L. 1934. Studies on the Structure of the Cerebral Cortex. II. Continuation of the Study of the Ammonic System. *J. Psychol. Neurol.* 46:113–177.
- Dodd, J., and J.S. Kelly. 1981. The actions of cholecystokinin and related peptides on pyramidal neurones of the mammalian hippocampus. *Brain Res.* 205:337–350. [https://doi.org/10.1016/0006-8993\(81\)90344-9](https://doi.org/10.1016/0006-8993(81)90344-9)
- Dodd, J., R. Dingleline, and J.S. Kelly. 1981. The excitatory action of acetylcholine on hippocampal neurones of the guinea pig and rat maintained in vitro. *Brain Res.* 207:109–127. [https://doi.org/10.1016/0006-8993\(81\)90682-X](https://doi.org/10.1016/0006-8993(81)90682-X)
- Dudek, S.M., G.M. Alexander, and S. Farris. 2016. Rediscovering area CA2: unique properties and functions. *Nat. Rev. Neurosci.* 17:89–102. <https://doi.org/10.1038/nrn.2015.22>
- Evans, P.R., P. Parra-Bueno, M.S. Smirnov, D.J. Lustberg, S.M. Dudek, J.R. Hepler, and R. Yasuda. 2018. RGS14 Restricts Plasticity in Hippocampal CA2 by Limiting Postsynaptic Calcium Signaling. *eNeuro.* 5: ENEURO.0353-17.2018
- Fischer, Y. 2004. The hippocampal intrinsic network oscillator. *J. Physiol.* 554: 156–174. <https://doi.org/10.1113/jphysiol.2003.055558>
- Greene, D.L., S. Kang, and N. Hoshi. 2017. XE991 and Linopirdine Are State-Dependent Inhibitors for Kv7/KCNQ Channels that Favor Activated Single Subunits. *J. Pharmacol. Exp. Ther.* 362:177–185. <https://doi.org/10.1124/jpet.117.241679>
- Gu, N., K. Vervaeke, and J.F. Storm. 2007. BK potassium channels facilitate high-frequency firing and cause early spike frequency adaptation in rat CA1 hippocampal pyramidal cells. *J. Physiol.* 580:859–882. <https://doi.org/10.1113/jphysiol.2006.126367>
- Gullledge, A.T., and Y. Kawaguchi. 2007. Phasic cholinergic signaling in the hippocampus: functional homology with the neocortex? *Hippocampus.* 17:327–332. <https://doi.org/10.1002/hipo.20279>
- Hackelberg, S., and D. Oliver. 2018. Metabotropic Acetylcholine and Glutamate Receptors Mediate PI(4,5)P₂ Depletion and Oscillations in Hippocampal CA1 Pyramidal Neurons in situ. *Sci. Rep.* 8:12987. <https://doi.org/10.1038/s41598-018-31322-8>
- Haj-Dahmane, S., and R. Andrade. 1996. Muscarinic activation of a voltage-dependent cation nonselective current in rat association cortex. *J. Neurosci.* 16:3848–3861. <https://doi.org/10.1523/JNEUROSCI.16-12-03848.1996>
- Half, A.W., D. Gómez-Varela, D. John, and D.K. Berg. 2014. A novel mechanism for nicotinic potentiation of glutamatergic synapses. *J. Neurosci.* 34:2051–2064. <https://doi.org/10.1523/JNEUROSCI.2795-13.2014>
- Hasselmo, M.E., and E. Schnell. 1994. Laminar selectivity of the cholinergic suppression of synaptic transmission in rat hippocampal region CA1: computational modeling and brain slice physiology. *J. Neurosci.* 14: 3898–3914. <https://doi.org/10.1523/JNEUROSCI.14-06-03898.1994>
- Hitti, F.L., and S.A. Siegelbaum. 2014. The hippocampal CA2 region is essential for social memory. *Nature.* 508:88–92. <https://doi.org/10.1038/nature13028>
- Hönigsperger, C., M. Marosi, R. Murphy, and J.F. Storm. 2015. Dorsoventral differences in Kv7/M-current and its impact on resonance, temporal summation and excitability in rat hippocampal pyramidal cells. *J. Physiol.* 593:1551–1580. <https://doi.org/10.1113/jphysiol.2014.280826>
- Hu, W., and B.P. Bean. 2018. Differential Control of Axonal and Somatic Resting Potential by Voltage-Dependent Conductances in Cortical Layer 5 Pyramidal Neurons. *Neuron.* 97:1315–1326.e3. <https://doi.org/10.1016/j.neuron.2018.02.016>
- Jochems, A., and M. Yoshida. 2013. Persistent firing supported by an intrinsic cellular mechanism in hippocampal CA3 pyramidal cells. *Eur. J. Neurosci.* 38:2250–2259. <https://doi.org/10.1111/ejn.12236>
- Kay, K., M. Sosa, J.E. Chung, M.P. Karlsson, M.C. Larkin, and L.M. Frank. 2016. A hippocampal network for spatial coding during immobility and sleep. *Nature.* 531:185–190. <https://doi.org/10.1038/nature17144>
- Knauer, B., A. Jochems, M.J. Valero-Aracama, and M. Yoshida. 2013. Long-lasting intrinsic persistent firing in rat CA1 pyramidal cells: a possible mechanism for active maintenance of memory. *Hippocampus.* 23: 820–831. <https://doi.org/10.1002/hipo.22136>
- Kremin, T., and M.E. Hasselmo. 2007. Cholinergic suppression of glutamatergic synaptic transmission in hippocampal region CA3 exhibits

- laminar selectivity: Implication for hippocampal network dynamics. *Neuroscience*. 149:760–767. <https://doi.org/10.1016/j.neuroscience.2007.07.007>
- Lee, S.E., S.B. Simons, S.A. Heldt, M. Zhao, J.P. Schroeder, C.P. Vellano, D.P. Cowan, S. Ramineni, C.K. Yates, Y. Feng, et al. 2010. RGS14 is a natural suppressor of both synaptic plasticity in CA2 neurons and hippocampal-based learning and memory. *Proc. Natl. Acad. Sci. USA*. 107:16994–16998. <https://doi.org/10.1073/pnas.1005362107>
- Levey, A.I., S.M. Edmunds, V. Koliatsos, R.G. Wiley, and C.J. Heilman. 1995. Expression of m1-m4 muscarinic acetylcholine receptor proteins in rat hippocampus and regulation by cholinergic innervation. *J. Neurosci*. 15: 4077–4092. <https://doi.org/10.1523/JNEUROSCI.15-05-04077.1995>
- Liu, A.K.L., T.W. Chau, E.J. Lim, I. Ahmed, R.C.-C. Chang, M.E. Kalaitzakis, M.B. Graeber, S.M. Gentleman, and R.K.B. Pearce. 2019. Hippocampal CA2 Lewy pathology is associated with cholinergic degeneration in Parkinson's disease with cognitive decline. *Acta Neuropathol. Commun*. 7:61.
- MacVicar, B.A., and F.W. Tse. 1989. Local neuronal circuitry underlying cholinergic rhythmic slow activity in CA3 area of rat hippocampal slices. *J. Physiol*. 417:197–212. <https://doi.org/10.1113/jphysiol.1989.sp017797>
- Martinello, K., Z. Huang, R. Luján, B. Tran, M. Watanabe, E.C. Cooper, D.A. Brown, and M.M. Shah. 2015. Cholinergic afferent stimulation induces axonal function plasticity in adult hippocampal granule cells. *Neuron*. 85:346–363. <https://doi.org/10.1016/j.neuron.2014.12.030>
- McGehee, D.S., M.J.S. Heath, S. Gelber, P. Devay, and L.W. Role. 1995. Nicotine enhancement of fast excitatory synaptic transmission in CNS by presynaptic receptors. *Science*. 269:1692–1696. <https://doi.org/10.1126/science.7569895>
- McIntyre, C.K., L.K. Marriott, and P.E. Gold. 2003. Patterns of brain acetylcholine release predict individual differences in preferred learning strategies in rats. *Neurobiol. Learn. Mem*. 79:177–183. [https://doi.org/10.1016/S1074-7427\(02\)00014-X](https://doi.org/10.1016/S1074-7427(02)00014-X)
- McMahon, L.L., J.H. Williams, and J.A. Kauer. 1998. Functionally distinct groups of interneurons identified during rhythmic carbachol oscillations in hippocampus in vitro. *J. Neurosci*. 18:5640–5651.
- McQuiston, A.R. 2014. Acetylcholine release and inhibitory interneuron activity in hippocampal CA1. 1–7. *Front. Synaptic Neurosci*. 6:20.
- Mercer, A., K. Eastlake, H.L. Trigg, and A.M. Thomson. 2012. Local circuitry involving parvalbumin-positive basket cells in the CA2 region of the hippocampus. *Hippocampus*. 22:43–56. <https://doi.org/10.1002/hipo.20841>
- Mercer, A., H.L. Trigg, and A.M. Thomson. 2007. Characterization of neurons in the CA2 subfield of the adult rat hippocampus. *J. Neurosci*. 27: 7329–7338. <https://doi.org/10.1523/JNEUROSCI.1829-07.2007>
- Modi, B., D. Pimpinella, A. Paziotti, P. Zacchi, E. Cherubini, and M. Griguoli. 2019. Possible Implication of the CA2 Hippocampal Circuit in Social Cognition Deficits Observed in the Neuroligin 3 Knock-Out Mouse, a Non-Syndromic Animal Model of Autism. *Front. Psychiatry*. 10:513. <https://doi.org/10.3389/fpsy.2019.00513>
- Ochiishi, T., Y. Saitoh, A. Yukawa, M. Saji, Y. Ren, T. Shirao, H. Miyamoto, H. Nakata, and Y. Sekino. 1999. High level of adenosine A1 receptor-like immunoreactivity in the CA2/CA3a region of the adult rat hippocampus. *Neuroscience*. 93:955–967. [https://doi.org/10.1016/S0306-4522\(99\)00179-7](https://doi.org/10.1016/S0306-4522(99)00179-7)
- Oliva, A., A. Fernández-Ruiz, G. Buzsáki, and A. Berényi. 2016. Role of Hippocampal CA2 Region in Triggering Sharp-Wave Ripples. *Neuron*. 91: 1342–1355. <https://doi.org/10.1016/j.neuron.2016.08.008>
- Pagani, J.H., M. Zhao, Z. Cui, S.K.W. Avram, D.A. Caruana, S.M. Dudek, and W.S. Young. 2015. Role of the vasopressin 1b receptor in rodent aggressive behavior and synaptic plasticity in hippocampal area CA2. *Mol. Psychiatry*. 20:490–499. <https://doi.org/10.1038/mp.2014.47>
- Palacio, S., V. Chevaleyre, D.H. Brann, K.D. Murray, R.A. Piskorowski, and J.S. Trimmer. 2017. Heterogeneity in Kv2 Channel Expression Shapes Action Potential Characteristics and Firing Patterns in CA1 versus CA2 Hippocampal Pyramidal Neurons. *eNeuro*. 4:ENEURO.0267-17.2017.
- Piskorowski, R.A., K. Nasrallah, A. Diamantopoulou, J. Mukai, S.I. Hassan, S.A. Siegelbaum, J.A. Gogos, and V. Chevaleyre. 2016. Age-Dependent Specific Changes in Area CA2 of the Hippocampus and Social Memory Deficit in a Mouse Model of the 22q11.2 Deletion Syndrome. *Neuron*. 89: 163–176. <https://doi.org/10.1016/j.neuron.2015.11.036>
- Pitler, T.A., and B.E. Alger. 1990. Activation of the pharmacologically defined M3 muscarinic receptor depolarizes hippocampal pyramidal cells. *Brain Res*. 534:257–262. [https://doi.org/10.1016/0006-8993\(90\)90137-Z](https://doi.org/10.1016/0006-8993(90)90137-Z)
- Ransmayr, G., P. Cervera, E. Hirsch, M. Ruberg, L.B. Hersh, C. Duyckaerts, J.J. Hawc, C. Delumeau, and Y. Agid. 1989. Choline acetyltransferase-like immunoreactivity in the hippocampal formation of control subjects and patients with Alzheimer's disease. *Neuroscience*. 32:701–714. [https://doi.org/10.1016/0306-4522\(89\)90291-1](https://doi.org/10.1016/0306-4522(89)90291-1)
- Robert, V., S. Cassim, V. Chevaleyre, and R.A. Piskorowski. 2018. Hippocampal area CA2: properties and contribution to hippocampal function. *Cell Tissue Res*. 373:525–540. <https://doi.org/10.1007/s00441-017-2769-7>
- Rodríguez-Menchaca, A.A., S.K. Adney, L. Zhou, and D.E. Logothetis. 2012. Dual Regulation of Voltage-Sensitive Ion Channels by PIP(2). *Front. Pharmacol*. 3:170. <https://doi.org/10.3389/fphar.2012.00170>
- Shalinsky, M.H., J. Magistretti, L. Ma, and A.A. Alonso. 2002. Muscarinic activation of a cation current and associated current noise in entorhinal-cortex layer-II neurons. *J. Neurophysiol*. 88:1197–1211. <https://doi.org/10.1152/jn.2002.88.3.1197>
- Simons, S.B., Y. Escobedo, R. Yasuda, and S.M. Dudek. 2009. Regional differences in hippocampal calcium handling provide a cellular mechanism for limiting plasticity. *Proc. Natl. Acad. Sci. USA*. 106:14080–14084. <https://doi.org/10.1073/pnas.0904775106>
- Srinivas, K.V., E.W. Buss, Q. Sun, B. Santoro, H. Takahashi, D.A. Nicholson, and S.A. Siegelbaum. 2017. The Dendrites of CA2 and CA1 Pyramidal Neurons Differentially Regulate Information Flow in the Cortico-Hippocampal Circuit. *J. Neurosci*. 37:3276–3293. <https://doi.org/10.1523/JNEUROSCI.2219-16.2017>
- Stevenson, E.L., and H.K. Caldwell. 2014. Lesions to the CA2 region of the hippocampus impair social memory in mice. *Eur. J. Neurosci*. 40: 3294–3301. <https://doi.org/10.1111/ejn.12689>
- Stocker, M. 2004. Ca(2+)-activated K+ channels: molecular determinants and function of the SK family. *Nat. Rev. Neurosci*. 5:758–770. <https://doi.org/10.1038/nrn1516>
- Storm, J.F. 1988. Temporal integration by a slowly inactivating K+ current in hippocampal neurons. *Nature*. 336:379–381. <https://doi.org/10.1038/336379a0>
- Sun, Q., K.V. Srinivas, A. Sotayo, and S.A. Siegelbaum. 2014. Dendritic Na+ spikes enable cortical input to drive action potential output from hippocampal CA2 pyramidal neurons. *eLife*. 3:e04551. <https://doi.org/10.7554/eLife.04551>
- Tang, A.H., M.A. Karson, D.A. Nagode, J.M. McIntosh, V.N. Uebele, J.J. Reinger, M. Klugmann, T.A. Milner, and B.E. Alger. 2011. Nerve terminal nicotinic acetylcholine receptors initiate quantal GABA release from perisomatic interneurons by activating axonal T-type (Cav3) Ca2+ channels and Ca2+ release from stores. *J. Neurosci*. 31:13546–13561. <https://doi.org/10.1523/JNEUROSCI.2781-11.2011>
- Tirkko, N.N., K.W. Eyring, I. Carcea, M. Mitre, M.V. Chao, R.C. Froemke, and R.W. Tsien. 2018. Oxytocin Transforms Firing Mode of CA2 Hippocampal Neurons. *Neuron*. 100:593–608.e3. <https://doi.org/10.1016/j.neuron.2018.09.008>
- Tucker, M.S., I. Khan, R. Fuchs-Young, S. Price, T.L. Steininger, G. Greene, B.H. Wainer, and M.R. Rosner. 1993. Localization of immunoreactive epidermal growth factor receptor in neonatal and adult rat hippocampus. *Brain Res*. 631:65–71. [https://doi.org/10.1016/0006-8993\(93\)91187-W](https://doi.org/10.1016/0006-8993(93)91187-W)
- Vellano, C.P., S.E. Lee, S.M. Dudek, and J.R. Hepler. 2011. RGS14 at the interface of hippocampal signaling and synaptic plasticity. *Trends Pharmacol. Sci*. 32:666–674. <https://doi.org/10.1016/j.tips.2011.07.005>
- Velumian, A.A., L. Zhang, P. Pennefather, and P.L. Carlen. 1997. Reversible inhibition of IK, IAHP, Ih and Ica currents by internally applied gluconate in rat hippocampal pyramidal neurones. *Pflugers Arch*. 433: 343–350. <https://doi.org/10.1007/s004240050286>
- Williams, J.H., and J.A. Kauer. 1997. Properties of carbachol-induced oscillatory activity in rat hippocampus. *J. Neurophysiol*. 78:2631–2640. <https://doi.org/10.1152/jn.1997.78.5.2631>
- Woehler, A., K.H. Lin, and E. Neher. 2014. Calcium-buffering effects of gluconate and nucleotides, as determined by a novel fluorimetric titration method. *J. Physiol*. 592:4863–4875. <https://doi.org/10.1113/jphysiol.2014.281097>
- Wolfart, J., and J. Roeper. 2002. Selective coupling of T-type calcium channels to SK potassium channels prevents intrinsic bursting in dopaminergic midbrain neurons. *J. Neurosci*. 22:3404–3413. <https://doi.org/10.1523/JNEUROSCI.22-09-03404.2002>
- Yamamura, H.I., M.J. Kuhar, and S.H. Snyder. 1974. In vivo identification of muscarinic cholinergic receptor binding in rat brain. *Brain Res*. 80: 170–176. [https://doi.org/10.1016/0006-8993\(74\)90738-0](https://doi.org/10.1016/0006-8993(74)90738-0)
- Young, W.S., J. Li, S.R. Wersinger, and M. Palkovits. 2006. The vasopressin 1b receptor is prominent in the hippocampal area CA2 where it is unaffected by restraint stress or adrenalectomy. *Neuroscience*. 143:1031–1039. <https://doi.org/10.1016/j.neuroscience.2006.08.040>
- Yue, C., S. Remy, H. Su, H. Beck, and Y. Yaari. 2005. Proximal persistent Na+ channels drive spike afterdepolarizations and associated bursting in adult CA1 pyramidal cells. *J. Neurosci*. 25:9704–9720. <https://doi.org/10.1523/JNEUROSCI.1621-05.2005>
- Zhao, M., Y.-S. Choi, K. Obrietan, and S.M. Dudek. 2007. Synaptic plasticity (and the lack thereof) in hippocampal CA2 neurons. *J. Neurosci*. 27: 12025–12032. <https://doi.org/10.1523/JNEUROSCI.4094-07.2007>